



Dripta Dutta || Takeshi Imayama || Dyuti Prakash Sarkar || Kaushik Das

Creep behaviour of omphacite and amphibole-plagioclase symplectite: The role of heterogeneous hydration in the Tso Morari eclogite during retrogression

Dripta Dutta^{1,2*}, Takeshi Imayama¹, Dyuti Prakash Sarkar^{2,#}, Jun-ichi Ando², Kaushik Das²

ORCiD - 0000-0001-9247-6388 (Dripta Dutta), 0000-0002-7704-4963 (Takeshi Imayama), 0000-0001-7406-5956 (Dyuti Prakash Sarkar), 0000-0002-2372-2095 (Kaushik Das)

Abstract

Replacement reactions progress to varying degrees depending on the P-T conditions, exhumation rates, and fluid availability. The preservation of reactants and retrogressed products allows for the reconstruction of microstructural and mineralogical progression, which we investigated using electron backscattered diffraction and microprobe analyses on the omphacite, amphibole-plagioclase symplectite, and matrix amphibole of the Tso Morari eclogite. Elliptical shapes, absence of chemical zonation, and scarce subgrains suggest that omphacite grains deformed via body diffusion creep. Because of the heterogeneous distribution of externally derived hydrous fluids in the eclogite, the omphacite is replaced by amphibole-plagioclase symplectite either partially along the peripheries (S1 symplectite) or completely (S2 symplectite). Strong omphacite CPOs, caused by growth anisotropy, are inherited by the symplectite constituents such that $<0.01>_{Omp}//<0.01>_{Amp}//<0.01>_{Plag}$, $<0.10>_{Omp}//<0.01>_{Amp}//<0.01>_{Plag}$. Both generations of amphibole grains, i.e., in S1 and S2, crystallised during exhumation. The S1 amphibole grains are poorer in Si (6.75–7.34 apfu) and crystallised earlier than those in S2 (Si = 7.29–7.79 apfu). Elevated stresses at the reaction interfaces deformed the plagioclase in S1 via dislocation creep. In

¹ Institute of Frontier Science and Technology, Okayama University of Science, Okayama 700-0005, Japan

² Department of Earth and Planetary Systems Science, Hiroshima University, Higashi Hiroshima 739-8526, Japan

^{*} now at Division of Earth Sciences, Graduate School of Sciences and Technology for Innovation, Yamaguchi University, Yoshida 753-8512, Japan

^{*} Correspondence - dripta.dutta@gmail.com, ddutta@hiroshima-u.ac.jp (Dripta Dutta)

contrast, due to fluid abundance, the plagioclase in S2 deformed via diffusion creep-accommodated grain boundary sliding. The misorientations across the subgrain boundaries in the amphibole grains constituting S1 and S2 are similar to those in the amphibole of the eclogite matrix and the garnet amphibolites. The amphibole grains in S1, eclogite matrix, and garnet amphibolites deformed via dislocation creep, whereas dislocation-accommodated grain boundary sliding deformed those in S2. (242 words)

Keywords - CPO Inheritance, Deformation mechanism, Growth anisotropy, Dislocation creep, Diffusion creep, Dissolution-precipitation, Grain Boundary Sliding

Introduction

The exhumation velocity and its temporal variations, in addition to the pressure-temperature trajectory and fluid availability, greatly influence the textural features preserved in an exhumed terrane. Fast and near-isothermal decompression of ultra-high pressure (UHP) units, such as those reported from the Tso Morari region (India, St-Onge et al. 2013), Kaghan Valley (Pakistan, Parrish et al. 2006), Kokchetav Massif (Kazakhstan, Hermann et al. 2001), allows for the preservation of disequilibrium textures that are characterised by the presence of reactant(s) in contact with the products (Mørk 1985; Wayte et al. 1989; García-Casco and Torres-Roldán 1996; Peterman and Grove 2010; Gaidies et al. 2017; Ogilvie and Gibson 2017). Fast exhumation rates are comparable to horizontal plate velocities and can transport UHP units from peak to mid-crustal depths within 10 Ma (Gerya et al. 2002; Kylander-Clark et al. 2012; Warren 2013). Symplectite complexes typically consist of vermicular intergrowths of multiple secondary phases, which crystallised simultaneously due to the destabilisation of a primary phase caused by the changing pressure and/or temperature conditions (Spry 1969; Barker 1998). The omphacite in exhumed UHP eclogites, upon decompression, generally disintegrates into diopside-plagioclase symplectite, which gradually transforms into an amphibole-plagioclase aggregate due to retrogression in the presence of hydrous fluids (Martin and Duchêne 2015; Martin 2019). Partial breakdown of omphacite to amphiboleplagioclase symplectite due to late-stage hydrous fluid influx has also been observed (Massonne 2012). Symplectitisation also involves the inheritance of the crystallographic preferred orientations (CPOs) of the precursor parent phase by the daughter crystals (Heidelbach and Terry 2013; Spruzeniece et al. 2017; Zertani et al. 2024).

Deformation experiments have demonstrated that a diopside-plagioclase aggregate is weaker than pure clinopyroxene (Dimanov and Dresen 2005). Hydration and amphibole formation can further lower the bulk plastic strength of the aggregate (Marti et al. 2018). Thus, symplectitisation, which also involves grain size reduction, should naturally result in the rheological weakening of eclogites (Jamtveit et al. 2016; Zertani et al. 2024). A recent study

shows that the symplectite constituents in the UHP eclogite of the Western Gneiss Region (Norway) deformed via grain size-sensitive (GSS) creep (Zertani et al. 2024). Nevertheless, the deformation experiments by Mansard *et al.* (2020) demonstrate that the absence of interconnected layers of fine-grained reaction products could inhibit or impede bulk rock weakening. Although the reaction-induced decrease in the grain size and consequent switch to GSS creep is predicted to be more efficient during retrogression (Brodie and Rutter 1987), it is not impossible for the products of positively dilatant transformation reactions to experience intracrystalline plastic deformation via dislocations (Greenwood and Johnson 1965; White and Knipe 1978; Poirier 1982, 1985).

Despite the interrelationships between metamorphism and deformation, previous workers assessed either the geochemical (O'Brien 1993; Brodie 1995; Martin 2019) or microstructural (Odashima et al. 2007; Heidelbach and Terry 2013; Spruzeniece et al. 2017; Zertani et al. 2024) attributes of symplectite. Consequently, the mechanisms facilitating the deformation of symplectitic minerals at the initial and final stages of their growth in naturally deformed eclogites remain poorly understood. This contribution examines one eclogite and two garnet amphibolites from the Tso Morari region. In the eclogite, we investigated the deformation characteristics of the Na-rich clinopyroxene and the symplectitic minerals, which either partially or completely replaced the former. Additionally, we integrated the compositional and textural features of the symplectitic amphibole grains to reconstruct their sequential development and deformation. The CPOs and mineral chemistries of the symplectitic amphibole grains are also compared with those in the eclogite matrix and the garnet amphibolites to discern the characteristic variations with retrogression.

Geological Setting

The Tso Morari Crystallines (TMC) lies to the immediate south of the Indus Tsangpo suture zone (Fig. 1a). Structurally, the TMC is a northwesterly trending antiformal dome and forms

the footwall of the detachment faults that separate it from the surrounding lithounits, i.e., Nidar Ophiolite in the north and Tetragoal Nappe in the south (de Sigoyer et al. 2004; Buchs and Epard 2019) (Fig. 1b). The variably deformed granite gneiss, also known as the Tso Morari Gneiss or the Puga Gneiss, contain boudinaged metabasite (retrograded eclogite and garnet amphibolite) layers that occur nearly parallel to the gneissic foliations. The eclogite units of the TMC likely originated from the Permian basalt of the Panjal Traps (Spencer et al. 1995; Jonnalagadda et al. 2019) or the Early Cretaceous Ladakh ophiolites (Ahmad et al. 2022).

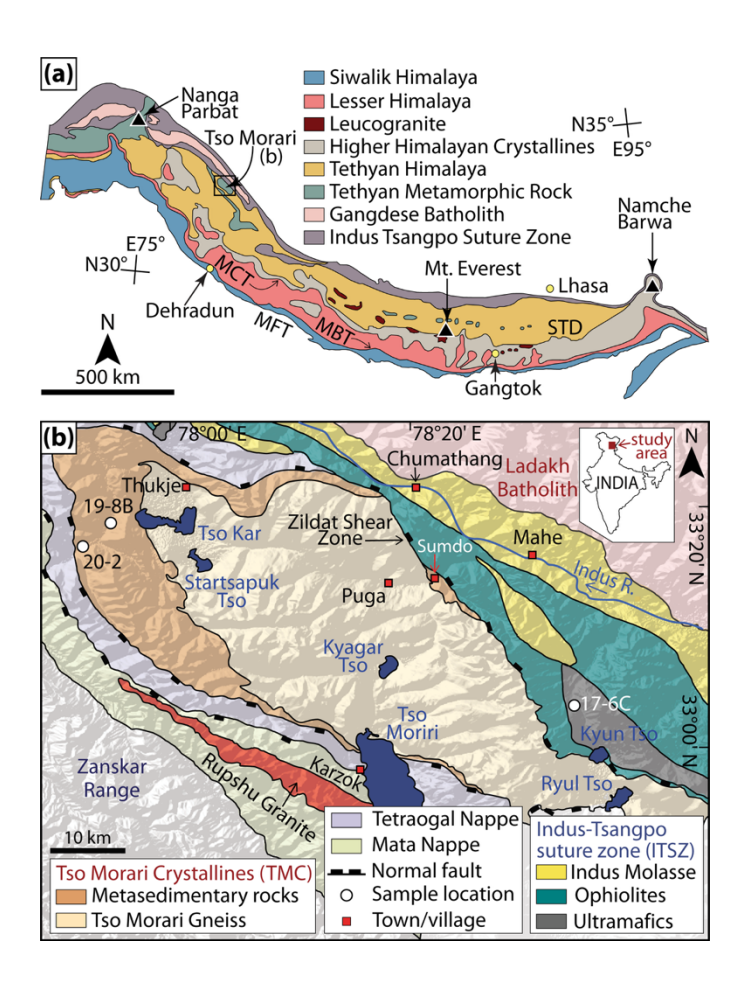


Fig. 1. Geological maps of the study area. (a) Geological map of the Himalayan orogen (reproduced from Dutta and Mukherjee, 2021). The yellow circles mark the locations of major cities/towns. The black triangles mark the major mountain peaks. The black unfilled square demarcates the study area. (b) Geological map of the Tso Morari region (redrawn after de Sigoyer et al., 2004 and Epard and Steck, 2008). White filled circles mark sample locations.

Recent trace element geochemistry and U-Pb geochronology show that Early Paleozoic bimodal and multi-stage magmatism in a continental rift produced the protoliths of the TMC gneiss and metabasite (Imayama et al. 2024). The protolith to the eclogite boulder (17-6C, Fig.

1a) from the north of the Zildat Shear Zone could have been an island-arc basalt instead (Imayama et al. 2024). Previous studies have identified mineral assemblages corresponding to the prograde path (e.g., St-Onge et al., 2013), eclogite-facies peak metamorphism (de Sigoyer et al. 1997; Wilke et al. 2015; Dey et al. 2023), granulite facies thermal peak (St-Onge et al. 2013; Chatterjee and Jagoutz 2015), and amphibolite-facies retrogression (Mukherjee et al. 2003; Chatterjee and Jagoutz 2015) from the metabasites (Table ST1 in Supplementary File S2). These studies suggest that the TMC rocks subducted to at least 70 km of depth, experienced a thermal maximum during their nearly isothermal decompression, and exhumed along a higher thermal gradient after the peak temperature. Epard and Steck (2008) reported that oriented relics of omphacite in the eclogite are rare and, therefore, proposed that the eclogite facies or UHP deformation was weak and characterised by static recrystallisation of omphacite. In contrast, de Sigoyer et al. (1997, 2004) proposed that the peak pressure deformation (2.3 GPa and 580 ± 60 °C) at ~ 55 Ma caused the omphacite in the eclogite to recrystallise dynamically and develop the preferred alignment.

Analytical methods

Three non-oriented samples, 17-6C, 19-8B, and 20-2, are studied (Fig. 1b). Sample 17-6C is an eclogite (fig. SF1 in the Supplementary File S1) collected from the north of the Zildat Shear Zone. The garnet amphibolite samples 19-8B and 20-2 are collected from within the metasedimentary sequence that mantles the Tso Morari Gneiss. Samples 17-6C and 19-8B are non-foliated and, therefore, sliced along random directions to prepare the thin sections. The weakly foliated sample 20-2 lacks clear lineation and, therefore, is cut along the dip direction and perpendicular to the foliation. Rock chips (1.3 cm × 1.3 cm in area and 0.5 cm thick), one each from samples 17-6C, 20-2, and 19-8B, are sliced using the Buehler IsoMet Low-Speed Saw. The analysed surfaces of the rock chips of samples 19-8B and 20-2 are

parallel to their respective thin sections. The thin sections and the rock chips were carboncoated before BSE imaging and electron microprobe analysis.

Thin section petrography and backscattered electron imaging

The thin sections are used to perform the preliminary petrographic study with a polarizing microscope. Backscattered electron (BSE) images are acquired from the rock chips using the JEOL JXA-8230 electron probe microanalyzer at the Okayama University of Science, Japan. For BSE imaging, the working distance, beam current, and acceleration voltage are set to 11 mm, 12 nA, and 15 kV, respectively.

Electron microprobe analysis

Mineral chemistry data are obtained from the thin sections and the rock chips using the JEOL JXA-8230 electron probe microanalyzer at the Okayama University of Science, Japan. The rock chips are used to determine the mineral chemistries of the grains present at the exact locations mapped using the EBSD. The working conditions are the same as those used during BSE imaging. We used a beam spot size of 3 μ m for the measurements. Routine analytical calibration is performed using natural and synthetic samples of the following silicates and oxides. Oxides of nine elements – Si, Al, Ti, Fe, Mn, Mg, Ca, Na, and K – are measured in wavelength dispersive X-ray spectrometry modes by acquiring the following X-ray lines – Si $K\alpha$, Al $K\alpha$, Ti $K\alpha$, Fe $K\alpha$, Mn $K\alpha$, Mg $K\alpha$, Ca $K\alpha$, Na $K\alpha$, and K $K\alpha$. The ZAF correction algorithm is followed to perform the matrix corrections. An X-ray map is acquired from the thin section of sample 17-6C to check whether the clinopyroxene grains are zoned. The intensities of Al, Ca, Fe, Mg, Na, and Si for clinopyroxene and symplectite in the map are simultaneously measured using a 15 kV accelerating voltage and a 25 nA beam current.

Mineral chemistries of amphibole grains in the eclogite matrix are studied from the rock chips. The amphibole and plagioclase constituting the symplectite and the adjacent clinopyroxene are targeted in the thin section and the chips of 17-6C. In 19-8B and 20-2,

mineral chemistries of the amphibole are analysed from the respective rock chips. The clinopyroxene structural formula is normalized to four cations and six oxygens. For amphibole, the normalization assumes that the M4 site does not contain Mg, Fe, or Mn, and Si + Al + Ti + Mg + Fe + Mn = 13 (Stout 1972; Droop 1987). The plagioclase structural formula is recalculated based on eight oxygens.

Electron backscattered diffraction (EBSD) study

The EBSD data are acquired from the rock chips. Final polishing of the chips is carried out for four hours with 0.05 µm colloidal silica suspension using a vibratory polisher, following which they are coated with Osmium. EBSD mapping is carried out at the Department of Earth and Planetary Systems Science, Hiroshima University, Japan, using JEOL JSM-6390A SEM, equipped with a Nordlys EBSD detector and the AZtec software package (Oxford Instruments), at an accelerating voltage of 15 kV, working distance of 22 mm, pattern acquisition time of 96–146 ms, and a sample tilt of 70°.

EBSD mapping is performed in five regions (Sites 1S, 1S-A, 2S, 5M, and 7M) of the eclogite sample 17-6C (fig. SF2 in Supplementary File S1). Site 1S is the largest among them. It contains multiple coarse clinopyroxene grains with similarly oriented long axes that are targeted for EBSD. Therefore, it is mapped using a step size of 3 μ m. Two EBSD maps target the symplectite regions – Sites 1S-A (lies within Site 1) and 2S, targeting the symplectite categories S1 and S2, respectively. Sites 1S-A and 2S have smaller areas than Site 1S and are mapped at 1 μ m step size. The symplectite regions are selected from locations that contain fewer or are located near the clinopyroxene grains with their long axes oriented nearly parallel to those in Site 1S. Site 5M focuses on the matrix amphibole adjacent to a garnet porphyroblast. It is mapped at a step size of 2 μ m. A coarse quartz (Site 7M) from the eclogite matrix is mapped using a step size of 1 μ m to better detect the intragranular orientation variations. This dataset has also been used to estimate the flow stresses using the subgrain size piezometer of Goddard et al. (2020). We used a misorientation threshold (sg_min and

cutoff) of 1°, Burgers Vector of 5.1 × 10⁻⁴ μm, Shear Modulus of 4 × 10⁴ MPa, and a maximum number of 40 intercepts (nx_max). An amphibole-rich region is mapped from the garnet amphibolite sample 19-8B at a step size of 3 μm. In sample 20-2, we mapped two adjacent regions composed of elongated amphibole using step sizes of 2 μm. These regions are stitched together using the HKL Channel 5 Map Stitcher software package. The garnet amphibolites are included in the study to examine the differences in texture, composition, and deformation mechanisms between their amphibole grains and those of the symplectite and the matrix in the eclogite. Some fine-grained clinopyroxenes in the symplectites are Ca-rich (diopsidic) (Table ST2 in the Supplementary File S2). They could not be indexed as a clinopyroxene phase separate from that of the more dominant Na-rich clinopyroxene during the EBSD mapping. Since the finer clinopyroxene is scarce in the symplectite and because this work focuses on the Na-rich clinopyroxene instead, we removed all the finer clinopyroxene from the symplectites while processing the EBSD data and did not analyse them further.

The raw EBSD data are post-processed using the MTEX toolbox 5.10.2 (Hielscher and Schaeben 2008) on a MATLAB 2024b platform. Cleaning the raw data during post-processing includes discarding poorly indexed pixels, i.e., those with mean angular deviations >1.5° and grains with fewer than five pixels. Grain reconstruction is performed using the Voronoi decomposition algorithm in MTEX (Bachmann et al. 2011). 10° is chosen as the threshold misorientation angle to define the grain boundaries. The Dauphine twin boundaries in quartz grains have been merged. The orientation distribution functions used to plot the pole figures are calculated using a de la Vallée Poussin kernel halfwidth of 10°. The pole figures for the symplectite regions are presented as lower hemisphere projections on equal-area nets using orientation data from all the indexed pixels, which are coloured as per the orientation colouring scheme (IPF key) of the corresponding mineral to ease the visual inspection of the orientation relationships between the grains of different phases. We use the one-point-pergrain scheme to plot the rest of the pole figures. The strengths of the crystallographic preferred

orientations (CPOs) are reported only for those that are contoured using the misorientation index (Skemer et al. 2005).

Intragranular or low-angle (2 to <10°) misorientation axis distributions are plotted for subgrain boundaries longer than 5 pixels. Maps illustrating the relative misorientation of each pixel within a grain to the mean orientation of the grain (mis2mean) are generated to determine the extent of intragranular plastic deformation. Misorientation profiles are constructed along line segments within selected grains of omphacite, amphibole, plagioclase, and quartz to quantify the misorientations across the subgrain boundaries. We used the MTEX-based script of Sikdar *et al.* (2023) for this.

Results

Petrography

Sample 17-6C

The eclogite consists of garnet, omphacite, amphibole, quartz, phengite, carbonate minerals, rutile, and zoisite. The garnet porphyroblasts are euhedral. Their diameters range from 0.04 to 3 mm (Fig. 2a). Most of them contain microfractures filled with amphibole, white mica, with or without quartz (fig. SF3a in Supplementary File S1). The omphacite grains are coarse, with equivalent diameters ranging between 0.1 mm and 0.6 mm. They have elliptical outlines with aspect ratios between 2 and 28. They occur as clusters and mostly in the vicinity of the garnet porphyroblasts. Within each cluster, they exhibit a strong shape-preferred orientation (Fig. 2b,c). Some omphacite grains contain transgranular microfractures characterised by parallel walls, minor dilation, and negligible shear displacement parallel to the walls (Fig. 2c,d). Many of these microfractures are filled with symplectites. (Fig. 2c,d). The quartz grains in the matrix exhibit conspicuous subgrain boundaries and fluid inclusion trails (Fig. 2e,f). Although the quartz-quartz boundaries are

generally curved, with evident grain boundary migration (Fig. 2f), some are much straighter (fig. SF3b in Supplementary File S1). Prismatic amphibole grains occur at boundaries of the garnet porphyroblasts (Fig. 2c) and away from them, with the latter being coarser (Fig. 2g). Coarse white mica is also present in the matrix (Fig. 2h).

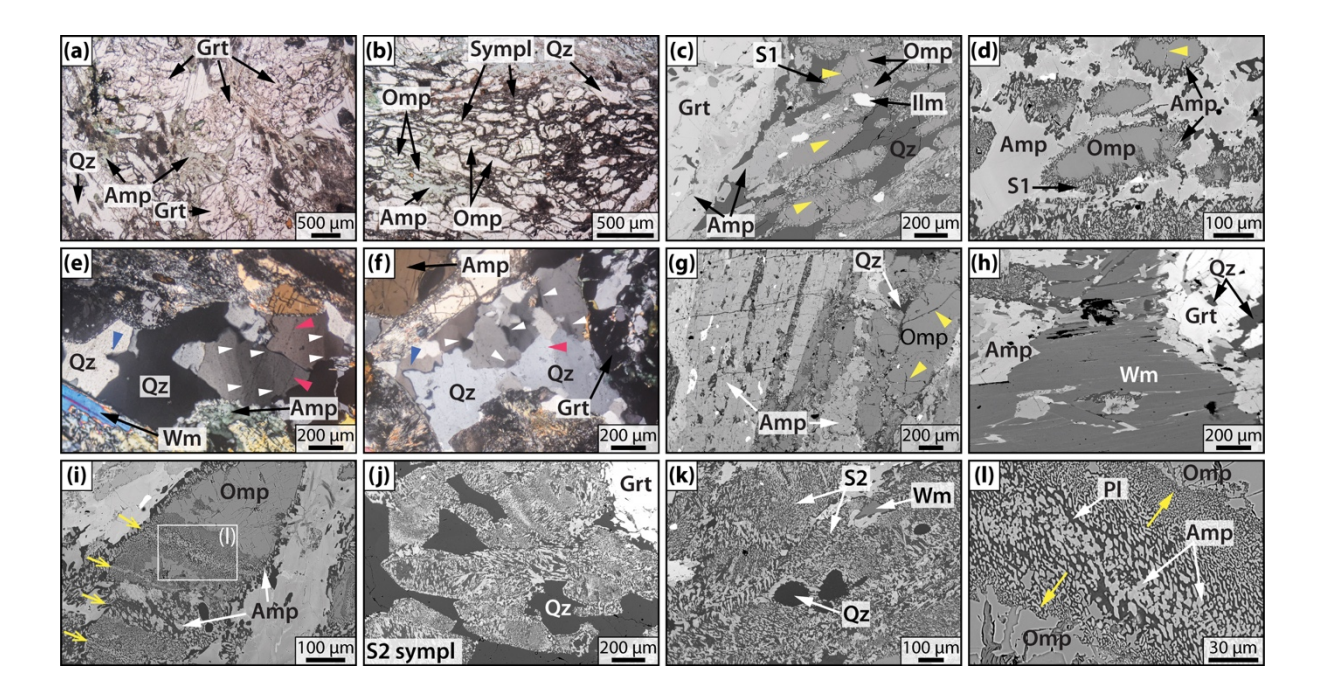


Fig. 2. Transmitted light photomicrographs and BSE images from sample 17-6C. (a) Euhedral garnet porphyroblasts along with quartz and amphibole grains in the matrix (plane-polarized light). (b) Preferentially aligned, elliptical omphacite grains surrounded by symplectitic regions and matrix amphibole (plane-polarized light). (c) Omphacite grains in a matrix of quartz grains near a garnet porphyroblast in the eclogite. Retrograde amphibole grains are present at the margin of the garnet porphyroblast. The omphacite grains are surrounded by symplectites (type S1), and most of them are fractured (yellow arrowheads). (d) Islands of partly symplectitised (type S1) omphacite within the amphibole matrix. (e,f) Cross-polarized photomicrographs of deformed quartz in the matrix with prominent subgrain boundaries (white arrowheads) and fluid inclusion trails (pink arrowheads). Migrated grain boundaries (blue arrowheads) are also visible. (g) Coarse and prismatic amphibole beside omphacite. (h) Coarse grains of white mica in the matrix alongside amphibole and garnet porphyroblast, with the latter containing inclusions of quartz. (i) Symplectitisation along the periphery of and across the omphacite grain. The thick bands of symplectite are nearly perpendicular to the long axis of the omphacite grains. The thinner linear stripes of coarse amphibole grains marked with the yellow arrows likely represent the original position of the fractures along which symplectitisation initiated. (j) The shapes of the former omphacite grains are preserved despite their complete replacement by symplectite (type S2). (k) Pervasive symplectitisation (type S2) with little trace of the precursor omphacite grains. (I) Zoomed-in image of (i) illustrating the gradual decrease in the amphibole grain sizes (yellow arrows) away from the initial position of the fracture. Mineral abbreviations are after Whitney and Evans (2010). The yellow arrowheads in (c), (d), and (g) point to the fractures.

The eclogite contains abundant symplectite. These are characterised by the granular intergrowths of amphibole and plagioclase, sometimes together with fine clinopyroxene grains. Depending upon the extent of omphacite replacement, three kinds of symplectite occurrences are observed in the eclogite – (i) partial replacement of the omphacite only along their peripheries (S1) (Fig. 2c,d), (ii) partial replacement along narrow zones across the omphacite (Fig. 2h), and (iii) complete replacement (S2), either with (Fig. 2j) or without (Fig. 2k) precursor grain shape preservation. Some of the coarser amphibole grains in S1 have their long axes perpendicular to the adjacent omphacite boundary (fig. SF3c in Supplementary File S1). The amphibole grains in S2 are coarser at the peripheries than those towards the cores of the omphacite (Fig. 2j). Similarly, in the case of symplectites occupying narrow zones across omphacite, the amphibole grain sizes decrease towards the omphacite interfaces. (Fig. 2l). The coarser amphibole grains in all the symplectites are relatively more euhedral than the finer ones (Fig. 2i–l).

Sample 19-8B

The garnet amphibolite is characterised by the mineral assemblage amphibole, plagioclase, garnet, quartz, ilmenite, and titanite. Plagioclase and quartz occur as isolated patches surrounded by amphibole (fig. SF4a,b in Supplementary File S1). Subgrain boundary is present in some coarser quartz grains (fig. SF4c in Supplementary File S1). Garnet porphyroblasts as well as ilmenite and titanite grains are more abundant than in sample 20-2 (fig. SF4a in Supplementary File S1).

Sample 20-2

The overall mineral assemblage is the same as that of sample 19-8B. The amphibole grains are euhedral and prismatic. They exhibit a strong shape-preferred orientation. Their overall arrangement defines the foliation, which is often deflected around the garnet porphyroblasts and, at some places, around the eye-shaped domains of plagioclase feldspar and quartz (fig. SF4d in Supplementary File S1). Most of the quartz grains are finer

than the amphibole grains and their long axes are oriented parallel to the foliation. Some of the coarser ones exhibit subgrain boundaries (fig. SF4e in Supplementary File S1), which are less prominent than those in the eclogite matrix. The amphibole-rich layers are separated by those of euhedral and granular plagioclase feldspar and quartz (fig. SF4f in Supplementary File S1). The garnet porphyroblasts are present in both amphibole-rich and plagioclase-rich layers. The coarser ones occur in the latter (fig. SF4f in Supplementary File S1).

Mineral chemistry

Eclogite (sample 17-6C)

The coarse and elliptical clinopyroxene grains are Ca-Na clinopyroxene in composition (Table ST2 in the Supplementary File S2). The Na contents of these grains lie within 0.53–0.57 apfu. They plot in the omphacite field of the clinopyroxene classification diagram of Morimoto (1989) (fig. SF5a in Supplementary File S1). Ca-rich clinopyroxenes are very few. They are fine-grained and occur within the symplectite. Two such grains are analysed. They are diopside in composition with Na contents of 0.18 and 0.25 apfu (fig. SF5b in Supplementary File S1). The plagioclase in the symplectite is albite to oligoclase (Ab_{88.8–99.3} An_{0.6–10.5} Or_{0.1–0.7}) (fig. SF5c and Table ST3 in Supplementary File S2).

The amphibole grains in the eclogite show a wide range of compositions (Table ST4 in Supplementary File S2). Those in the matrix (Amp-M) mostly plot in the Tschermakite field of the ^C(Al+Fe³⁺+2Ti) vs. ^A(2Ca+Na+K) classification diagram of Hawthorne et al. (2012) (Fig. 3a). The ^A(2Ca+Na+K) and ^C(Al+Fe³⁺+2Ti) contents lie within 0.14–0.70 apfu and 1.36–2.48 apfu, respectively. Their Si contents and Mg/(Mg+Fe²⁺) ratios range between 5.70–6.97 apfu and 0.62–0.97 (Fig. 3b). The ^BNa and ^TAl contents of the matrix amphibole grains range from 0.46–0.89 apfu and 1.03–2.30 apfu, respectively (Fig. 3c). Their ^C(Al+Ti+Fe³⁺) + ^A(Na+K) content varies from 1.81–2.83 apfu (Fig. 3d).

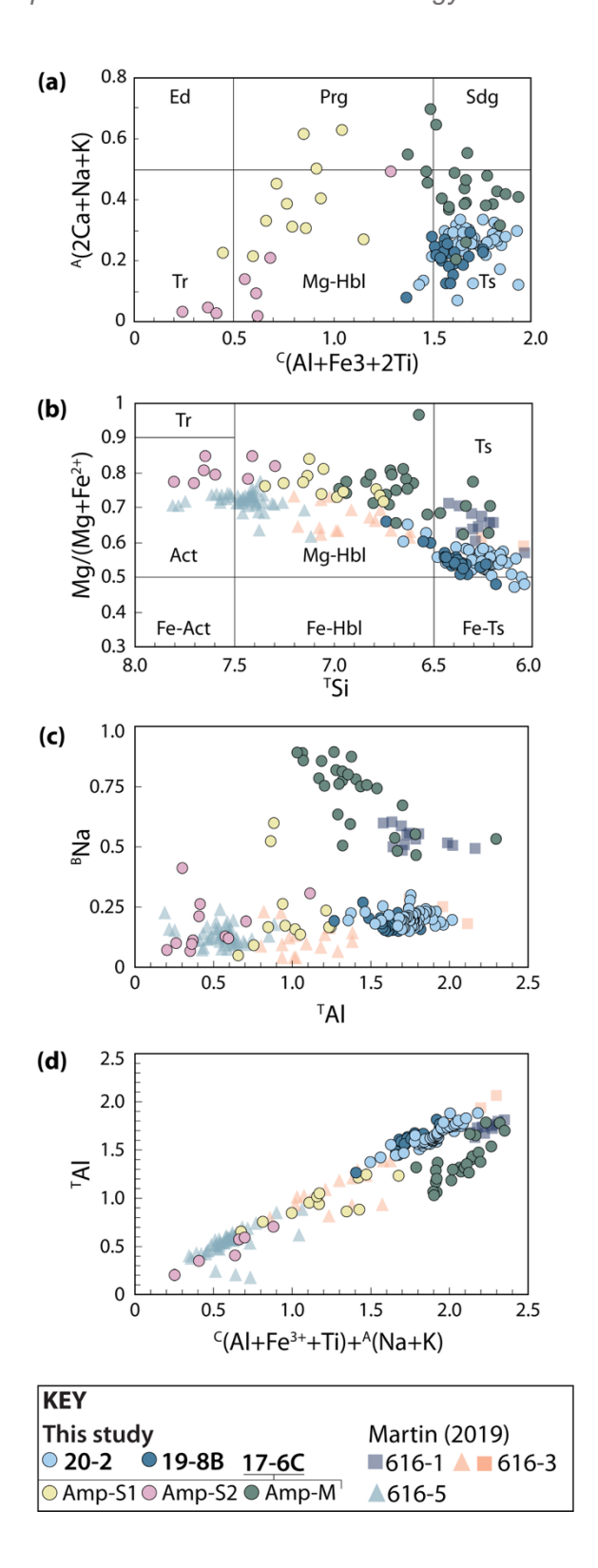


Fig. 3. EPMA-derived amphibole mineral chemistry data from the eclogite and garnet amphibolite samples. Classification diagrams for calcic amphibole **(a)** after Hawthorne et al. (2012) and **(b)** after Leake et al. (1997). Correlation plots of **(c)** Al_{total} (^TAl+^CAl) vs. ^BX_{Ca}, **(d)** ^C(Al+Fe³⁺+Ti) + ^A(Na+K) vs. ^TAl (Robinson et al. 1971), and **(e)** ^TAl v/s ^BNa (Brown 1977). Amp-S1 and Amp-S2 refer to the amphibole present in the two categories of symplectite, and Amp-M refers to the matrix amphibole. Abbreviations-: Fe-Act: ferro-actinolite, Fe-Hbl: ferro-hornblende, Fe-Ts: ferri-tschermakite, and Mg-Hbl: magnesiohornblende. The rest of the

mineral abbreviations are after Whitney and Evans (2010). Microprobe data of amphibole from the eclogites of the Western Gneiss Region (Norway) are also shown for easier comparison (Martin 2019). The mineral formula for this data is also recalculated based on 23 oxygens and 13 cations (excluding Ca, Na, and K). The triangles and squares correspond to the amphibole of the symplectite and matrix around the garnet porphyroblasts, respectively. The degree of retrogression and amphibole content of the symplectites increases from sample 616-1 to 616-3 to 616-5.

The amphibole grains in the two varieties of symplectite exhibit slightly variable compositions. Those constituting the S1 symplectite (Amp-S1) (Fig. 2d,e) have their ^A(2Ca+Na+K) and ^C(Al+Fe³⁺+2Ti) contents within 0.21–0.63 apfu and 0.47–1.21 apfu, respectively (Fig. 3a). The Si contents and Mg/(Mg+Fe²⁺) ratios of Amp-S1 range between 6.75–7.34 apfu and 0.72–0.84 (Fig. 3b). The ^C(Al+Fe³⁺+2Ti) contents for most of these are lower than Amp-M, whereas their Si contents are higher than Amp-M. The ^BNa (0.02–0.30 apfu) and ^C(Al+Ti+Fe³⁺) + ^A(Na+K) (0.70–1.72 apfu) contents are also lower than Amp-M (Fig. 3c,d). Compositionally, Amp-S1 mostly plot in the magnesiohornblende fields in the ^C(Al+Fe³⁺+2Ti) vs. ^A(2Ca+Na+K) (Hawthorne et al. 2012) and Si vs. Mg/(Mg+Fe²⁺) (Ca_A < 0.5) (Leake et al. 1997) classification diagrams. The amphibole grains of S2 symplectite (Amp-S2) exhibit A(2Ca+Na+K) and C(Al+Fe3+2Ti) contents of 0.02-0.50 apfu and 0.24-1.28 apfu, respectively (Fig. 3a). Their Si contents and Mg/(Mg+Fe²⁺) ratios range between 7.29 –7.79 apfu and 0.74–0.85 (Fig. 3b). The Na contents at the B-site and the ^C(Al+Ti+Fe³⁺) + ^A(Na+K) contents vary from 0.07-0.41 apfu and 0.28-1.77 apfu, respectively (Fig. 3c,d), both of which are lower than Amp-M. Amphibole compositions from the matrix and symplectite of the UHP eclogite of the Western Gneiss Region (Martin, 2019) match closely with those of sample 17/6C (Fig. 3d).

Garnet amphibolites (samples 19-8B and 20-2)

The amphibole in the two garnet amphibolite samples is compositionally similar (Tables ST5 and ST6 in Supplementary File S2). They mostly plot in the Tschermakite fields of the ^C(Al+Fe³⁺+2Ti) vs. ^A(2Ca+Na+K) and the Si vs. Mg/(Mg+Fe²⁺) classification diagrams of Hawthorne et al. (2012) and Leake *et al.*, (1997), respectively (Fig. 3a). The ^A(2Ca+Na+K) and

^C(Al+Fe³⁺+2Ti) contents of the amphibole of sample 20-2 vary between 0.07–0.33 apfu and 1.42–1.93 apfu, respectively, whereas those of sample 19-8B fall within the range 0.08–0.30 apfu and 1.36–1.75 apfu, respectively. Although the ^C(Al+Fe³⁺+2Ti) contents are comparable to those of the eclogite matrix, they are much higher than those of the symplectite. The Si contents of the amphibole grains in samples 19-8B and 20-2 range within 5.98–6.65 apfu and 6.18–6.73 apfu, respectively, and are lower than most of the matrix amphibole and the amphibole that constitute the symplectites, of the eclogite (Fig. 3b). Similarly, the Mg/(Mg+Fe²⁺) ratio of the amphibole in both samples 19-8B and 20-2 lie within 0.47–0.66 and are lower than those of the eclogite (Fig. 3b). The amphibole of sample 19-8B and 20-2 show similar ^BNa (Fig. 3c) and ^C(Al+Ti+Fe³⁺) + ^A(Na+K) (Fig. 3d) contents that range within 0.15–0.30 apfu and 1.40–2.18 apfu, respectively. These values are lower than those of the matrix amphibole of sample 17-6C.

Petrofabric analysis

Crystallographic preferred orientations

The elliptical omphacite grains in Site 1S (Fig. 4a, fig. SF2a in Supplementary File S1) are distinctly oriented. But the lack of variations in the orientations within each grain is evident (Fig. 4b). The amphibole CPO distributions show that their <001> are concentrated at three isolated locations that are distributed along a girdle (Fig.5c). The <100> and <010> are also distributed along girdles at a low angle to one another. The pole figures for this region demonstrate that the CPO distributions of the amphibole (Fig. 4c) nearly match those of the omphacite (Fig. 4d).

At Site 1S-A (Fig. 4e,f, fig. SF2b in Supplementary File S1), the CPO distributions of amphibole (Fig. 4g) and the omphacite (Fig. 4h) are also nearly similar. However, unlike Site 1S, the three axes of the amphibole and omphacite exhibit point maxima. Within Site 1S-A, the plagioclase <001> and <010> (Fig. 4i) exhibit point maxima, whereas the <100> are distributed along a girdle that is nearly parallel to the plane on which the long axis of the

omphacite at the centre (Fig. 4e) lies. Moreover, the plagioclase <001> and <010> in Site 1S-A are almost parallel to the <100> and <001>, respectively, of the omphacite and amphibole and the omphacite long axes.

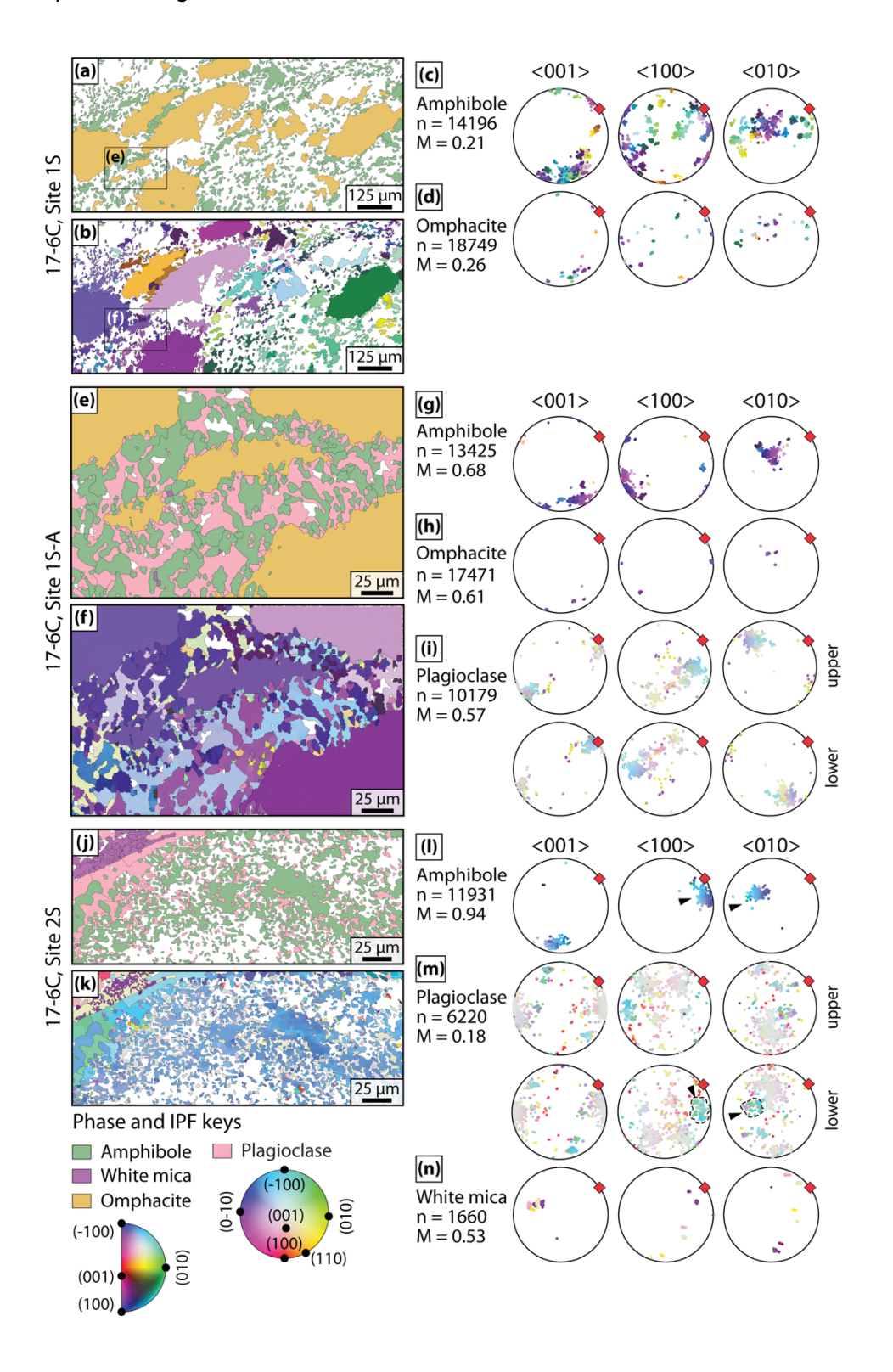


Fig. 4. Phase maps, orientation (IPF-X) maps, and mineral CPOs from the symplectite regions of sample 17-6C. (a), (e), and (j) are the phase maps for Site 1S, Site 1S-A, and Site 2S,

respectively. (b), (f), and (k) are the orientation maps for Site 1S, Site 1S-A, and Site 2S, respectively. All orientation data points are plotted in the pole figures. Each data point in the pole figures is coded according to the orientation colour scheme (IPF key) of the corresponding mineral provided at the bottom left. The pole figures are presented as equal area, lower hemisphere projections (except for plagioclase, for which the upper hemisphere projections are also shown). The red diamonds at the peripheries of the pole figures mark the mean orientation of the omphacite grains. n = number of orientation data points and M = misorientation index (Skemer et al. 2005).

Symplectite S2 (fig. SF2c in Supplementary File S1) lacks omphacite and mainly comprises fine-grained plagioclase in a coarse amphibole. A few white mica grains are present (Fig. 4j,k). The amphibole <001>, <010>, and <100> cluster at about the same region of the equal-area net as those of Site 1S-A (Fig. 4l). Although the plagioclase <001> and <010> are clustered and the <100> form a weak girdle, the overall distributions in the three pole figures are relatively weaker than that of Site 1S-A (Fig. 4m). In addition to the plagioclase <001> and <010> being parallel to the <100> and <001>, respectively, of the amphibole, some of the plagioclase grains have their <100> and <010> parallel to the those of some amphibole grains (marked with black arrowheads in Fig. 4l,m). The white mica <001> is clustered, whereas the <100> and <010> exhibit girdle distributions (Fig. 4n). Additional CPOs for the symplectite constituents are provided in fig. SF6 of the Supplementary File S1.

A few (<20) amphibole and white mica grains from the matrix of the eclogite sample 17-6C are mapped for EBSD data (fig. SF7a,b in Supplementary File S1). The amphibole <001> and <100> are clustered, whereas the <010> are distributed along a girdle (fig. SF7c in Supplementary File S1). The white mica <001> axes are concentrated at a point, but the <100> and <010> exhibit girdle distributions (fig. SF7d in Supplementary File S1).

The EBSD data from sample 19-8B is obtained from a region dominated by amphibole (Fig. 5e). Intragrain variations in amphibole are more prominent than those in quartz (Fig. 5f). The amphibole in this sample shows strong CPOs (Fig. 5g). The <001> CPO contains four isolated clusters, three of which lie on a girdle. The <100> CPO exhibits a point maximum as well. The <010> are distributed along a girdle parallel to the periphery and form a cluster near the center of the equal area net. The quartz CPOs are weak (Fig. 5h).

In sample 20-2, amphibole is dominant in the region mapped for EBSD data with much fewer quartz (Fig. 5e). Intragrain changes in orientations in the amphibole are visible in the orientation map (Fig. 5f). The CPO distributions of the amphibole (Fig. 5g) are relatively stronger than those of quartz (Fig. 5h). The amphibole <001> and <010> are distributed along girdles that are nearly parallel to the periphery of the equal area net. The CPO of the latter is relatively weaker than the former. The <100> are strongly clustered. The poles to quartz (0001), {11-20}, and {10-10}, on the other hand, do not exhibit any preferred orientation (Fig. 5h).

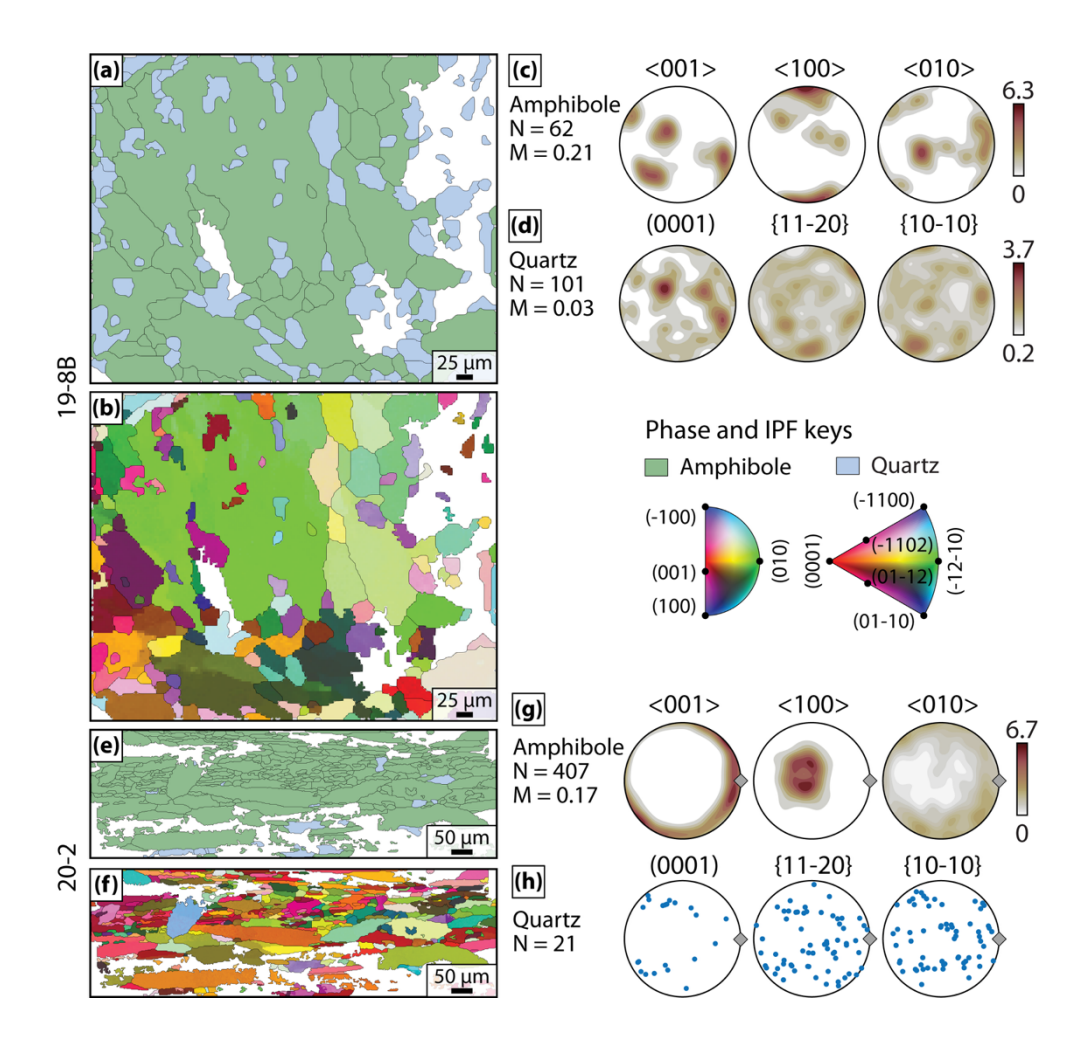


Fig. 5. Phase maps, orientation maps, and mineral CPOs from the garnet amphibolite samples. **(a)** and **(e)** are the phase maps for samples 19-8B and 20-2, respectively. **(b)** and **(g)** are the orientation maps for samples 19-8B and 20-2, respectively. The pole figures of **(c,d)** 19-8B and **(g,h)** 20-2 are presented as equal area, lower hemisphere projections. They are contoured to multiples of uniform density when at least 50 grains are present. The gray diamonds at the peripheries of the pole figures mark the mean orientation of the amphibole grains. The rest of the description is the same as that of Fig. 4.

Misorientation analysis

The low-angle (2–<10°) and correlated high-angle (≥10°) misorientation axes, henceforth referred to as LAXs and HAXs, respectively, of the amphibole in Site 1S-A show strong crystallographic control (Fig. 6a-c). The LAXs are mainly distributed along the (100) with the maxima parallel to <001> and <010> (Fig. 6a). The HAXs are preferentially oriented parallel to the <001> with two sub-maxima parallel to the poles to (100) and (-100) (Fig. 6b,c). The LAXs in the case of Site 2S are mainly distributed on (100) with a cluster parallel to <001>. But their overall distribution is weaker than that of Site 1S-A (Fig. 6d). The HAXs are more randomly distributed compared to those of Site 1S-A (Fig. 6e).

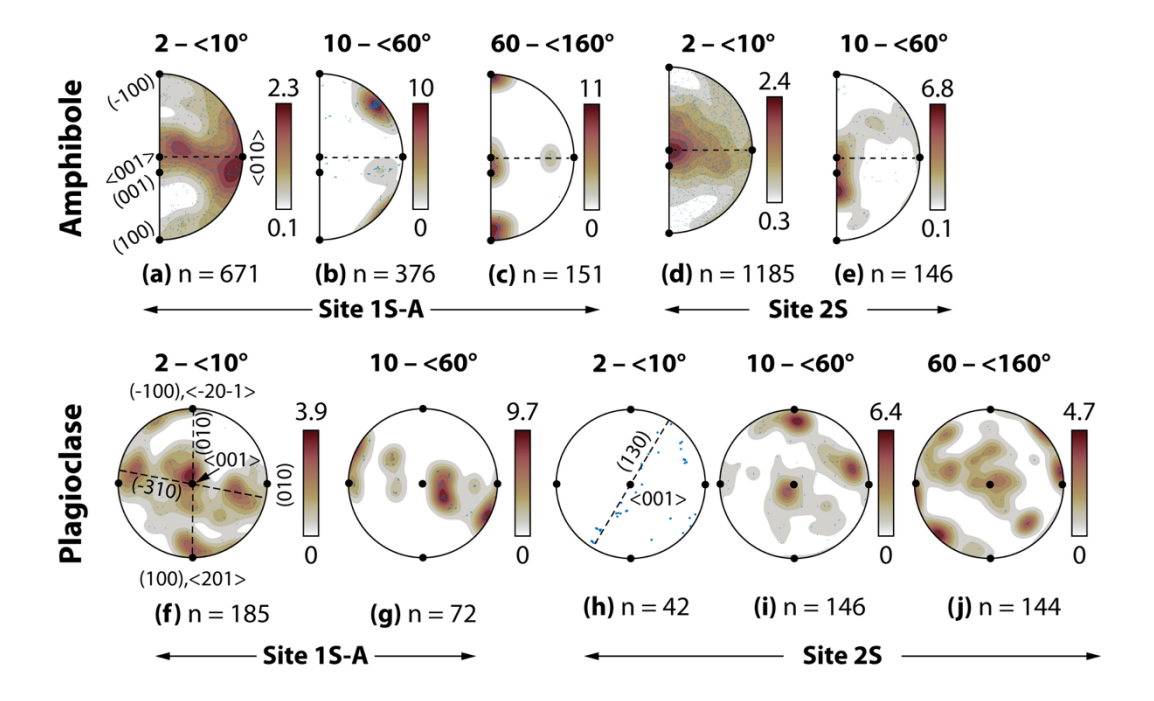


Fig. 6. Distributions of the low-angle (LAX, 2–<10°) and correlated high-angle (HAX, ≥10–160°) misorientation axes in crystal coordinate systems. Amphibole (a) LAXs and (b,c) HAXs from S1 symplectite. Amphibole (d) LAXs and (e) HAXs from S2 symplectite. Plagioclase (f) LAXs and (g) HAXs from S1 symplectite. Plagioclase (h) LAXs and (l,j) HAXs from S2 symplectite. The blue dots represent individual axis orientations, which are contoured to multiples of uniform density when at least 50 datapoints are present. The 'bilbao' colormap of Crameri (2018) is used. n = number of misorientation axes.

Plagioclase LAXs from Site 1S-A are present as isolated clusters in the crystal reference frame. These clusters are aligned along the (-310) and (010). The densest cluster occurs nearly parallel to the <001> (Fig. 6f). The HAXs of these plagioclase grains are mostly

either parallel to the <001> or perpendicular to the poles to (010) (Fig. 6g). Plagioclase LAXs from Site 2S are much fewer in number but are distributed mainly along the (130) (Fig. 6h). The HAXs, on the other hand, exhibit more random distributions compared to those of the amphibole and plagioclase of Site 1S-A (Fig. 6i,j).

The LAXs of amphibole and quartz from the eclogite matrix exhibit strongly preferred distributions in their respective crystal coordinate systems. Unlike the symplectite amphibole, the LAXs of matrix amphibole are parallel to their <-121>, which are nearly parallel to the poles to (-100). Some LAXs are parallel to the <001> (fig. SF8a in Supplementary File S1). The quartz LAXs are dominantly parallel to the <0001>. Some are parallel to the poles to (01-12), (01-11), (-1102), and (-1101) (fig. SF8b in Supplementary File S1). The amphibole LAXs of sample 19-8B are mostly distributed parallel to the (100) and strong clusters parallel to the <001> and nearly parallel to the <013> (fig. SF8c in Supplementary File S1). The HAXs are also preferentially oriented with maxima parallel to the <-100> and two sub-maxima parallel to the <013> and to the poles to (201) (fig. SF8d,e in Supplementary File S1). In sample 20-2, the amphibole LAXs (fig. SF8f in Supplementary File S1) are mostly parallel to the poles to (110) and (100), with relatively fewer being parallel to <001>. Their HAXs are strongly clustered parallel to <001> and perpendicular to the (100) in the crystal reference frame (fig. SF8g,h in Supplementary File S1).

The mis2mean maps and misorientation line profiles show that subgrains are scarce in omphacite but much more prominent in other minerals. Omphacite grains from Site 1S (Fig. 7a) show a maximum mis2mean value of 12° (Fig. 7b). The misorientation angle across the subgrain boundary is nearly 4° (Fig. 7c). A finer omphacite grain from Site 1S-A (Fig. 7d) has a maximum mis2mean value of 3.6° (Fig. 8e). The misorientation variation across the only subgrain boundary in this grain is slightly above 2° (Fig. 7f). Some of the plagioclase grains present in the symplectite of Site 1S-A (Fig. 8a) show relatively higher maxima of mis2mean values of 14° (Fig. 8b), 9° (Fig. 8c), and 9° (Fig. 8d) with the misorientations across some of the subgrain boundaries being >6° (Fig. 8e,f,g). The amphibole grains from the same

symplectite region show a mis2mean maximum of 13.7° (Fig. 9a). One of these grains with well-developed subgrain boundaries shows a maximum mis2mean value of 9° (Fig. 9b) with misorientations across the subgrain boundaries ranging between 5° to ~10° (Fig. 9c).

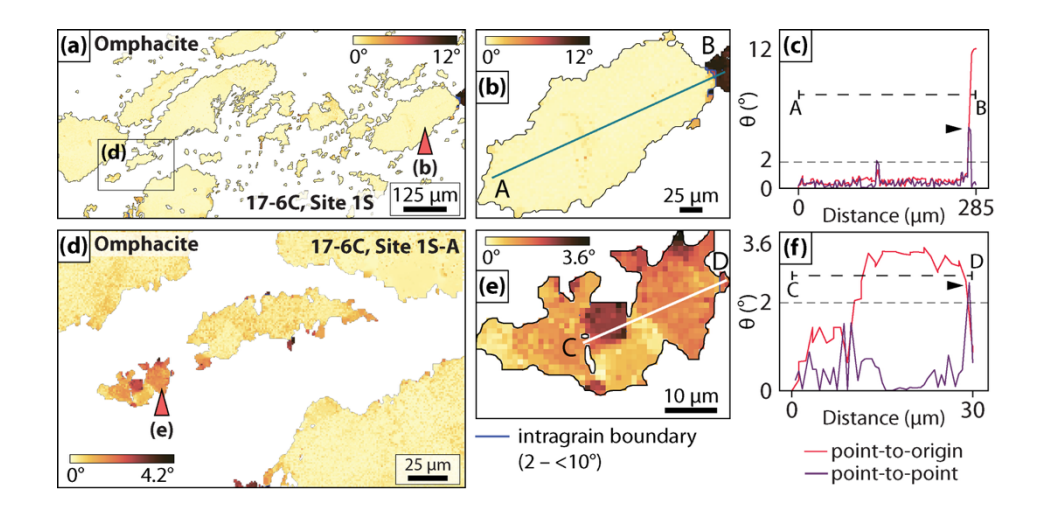


Fig. 7. mis2mean maps and misorientation profiles from sample 17-6C. (a) mis2mean map of omphacite from Site 1S. (b) mis2mean map and (c) misorientation profile of one of the omphacite grains (red arrowhead in (a)). (d) mis2mean map of the omphacite from Site 1S-A. (e) mis2mean map and (f) misorientation profile of one of the grains (red arrowhead in (d)). The black arrowheads in the misorientation profiles point to the misorientation angle peaks corresponding to the subgrain boundaries. The 'lajolla' colormap of Crameri (2018) is used for all the mis2mean maps. Each colour bar represents the angular range of misorientation of the corresponding map/grain.

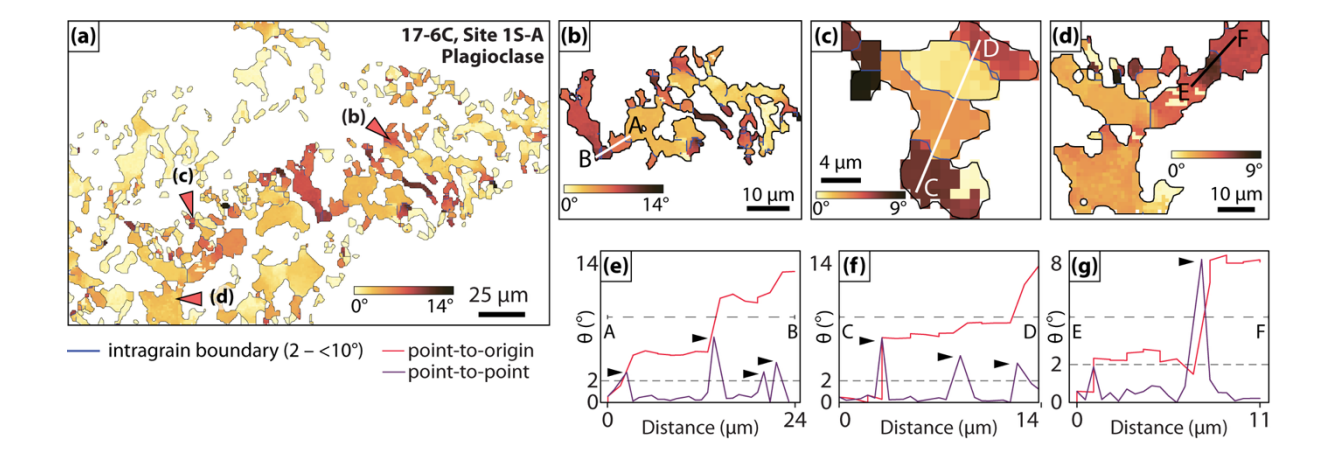


Fig. 8. mis2mean maps and misorientation profiles of selected plagioclase grains from sample 17-6C. **(a)** mis2mean map of plagioclase in the symplectite from Site 1S-A. **(b-d)** mis2mean maps of selected plagioclase grains (red arrowhead in **(a)**). Misorientation profiles along **(e)**

A-B, **(f)** C-D, and **(E-F)** line segments in the plagioclase grains of **(b)**, **(c)**, and **(d)**, respectively. The rest of the description is the same as that of Fig. 7.

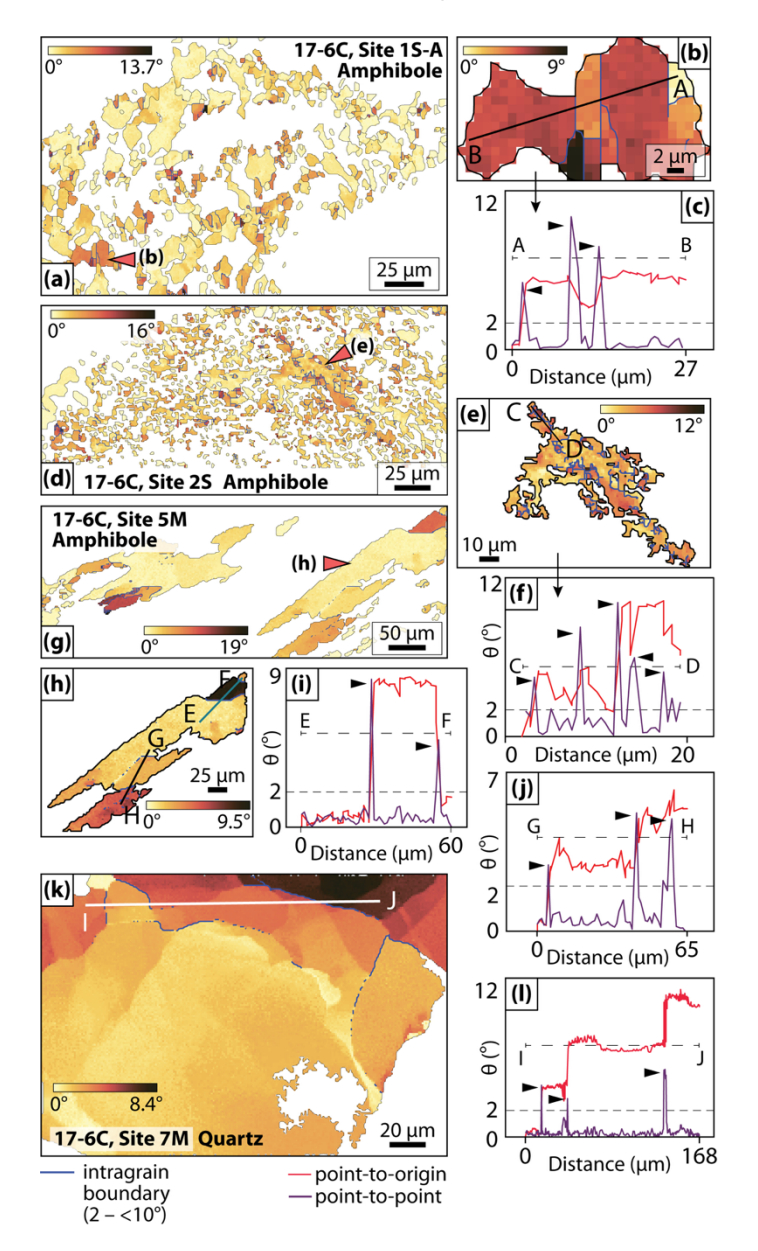


Fig. 9. mis2mean maps and misorientation profiles of selected grains from the eclogite sample 17-6C. mis2mean map of (a) all amphibole grains and (b) one selected amphibole grain (red arrowhead in (a)) from the S1 symplectite. (c) Misorientation profile along the A-B line segment in (b). (d) mis2mean map of amphibole in S2 symplectite. (e) mis2mean map of a selected amphibole grain (red arrowhead in (d)). The misorientation profile along the line segments C-D is illustrated in (f). (g) mis2mean map of amphibole from Site 5M. (h) mis2mean map of a selected amphibole grain (red arrowhead in (g)). The misorientation profiles along the line segments E-F and G-H are illustrated in (i) and (j), respectively. (k) mis2mean map of a quartz grain from Site 7M. (i) illustrates the misorientation profiles along the line segment I-J. The rest of the description is the same as that of Fig. 7.

Subgrains are present in some amphibole grains in the matrix of the eclogite (Fig. 9g). The maximum mis2mean value in one of these grains is 9.5° (Fig. 9h). The change in the misorientation angles across some of its subgrain boundaries are nearly 8° (Fig. 9i) and 5° (Fig. 9j). One of the quartz grains in the eclogite matrix consists of subgrain boundaries much longer than those preserved in the amphibole grains (Fig. 9k). The misorientations across these boundaries range within 3–6° (Fig. 9l). The amphibole grains in sample 19-8B also contain subgrains (fig. SF9a in Supplementary File S1). The misorientations across these range within 3–8° (fig. SF9b,c in Supplementary File S1). Subgrain boundaries are present in some of the amphibole grains in sample 20-2 (fig. SF9d–f in Supplementary File S1), with the misorientations across some of them being >8° (fig. SF9g–h in Supplementary File S1).

Quartz subgrain size piezometry

The subgrain size piezometry, with and without considering the friction coefficient correction of (Holyoke and Kronenberg 2010), generated flow stress values of 16.3 MPa and 13.5 MPa, respectively.

Discussion

Deformation characteristics of the symplectite and matrix constituents in the eclogite

Omphacite

Omphacite occurs as clusters of elliptical grains. Those within a cluster exhibit a clear shape preferred orientation, which reportedly developed at ~580 °C (de Sigoyer et al. 2004). Scarce and poorly developed subgrains (Fig. 7) indicate that the grains were weakly deformed in the dislocation creep regime. Previous thermobarometric (e.g., de Sigoyer et al., 1997; St-Onge et al., 2013) and EBSD-based CPO studies (Dutta and Mukherjee 2021; Dey et al. 2022) have shown that the eclogite and the enclosing granite gneiss of the Tso Morari region have experienced temperatures >600 °C. Given the insignificant dynamic recrystallization of the omphacite in sample 17-6C, post-deformation annealing at an elevated

temperature, such as the predicted thermal peak for the Tso Morari eclogite (620 to 725 °C, Table ST1 in Supplementary File S2) (Guillot et al. 1997; de Sigoyer et al. 1997; St-Onge et al. 2013; Wilke et al. 2015), could be responsible for limited subgrain development (Brenker et al. 2002). Alternatively, it could imply that the minimum flow stress of ~16–57 MPa (Zhang et al. 2006), required for dislocation creep in omphacite at the estimated thermal peak range of 620 to 725 °C and geological strain rate of 10⁻¹⁴ s⁻¹, was not reached.

Despite restricted subgrain development, omphacite exhibits clustered CPO distributions (Figs 5d,h). We infer that the omphacite CPOs have resulted from their anisotropic growth, which has previously been reported from eclogites (Godard and Van Roermund 1995; Mauler et al. 2001; Stöckhert 2002; Rogowitz and Huet 2021). The lack of chemically zoned omphacite grains in the studied eclogite (fig. SF10 in Supplementary File S1) suggests that volume diffusion or Nabarro-Herring creep produced the anisotropic crystals. Moreover, the grain-to-grain compositional variations (X_{Jd} = 0.39–0.44) noted for omphacite (Table ST2 in Supplementary File S2), despite the absence of compositional zoning, suggest that they grew under non-hydrostatic stress conditions (Hess and Ague 2024).

Brittle fractures are prominent in omphacite. Most of these transgranular fractures are parallel to the shorter axes of the grains (Fig. 2c,d,g). These fractures originated as Mode-I or extensional fractures because they do not exhibit shear displacement parallel to their walls (Paterson and Wong 2005). In some grains, the traces of (100), the common cleavage of omphacite (Deer et al. 2013), are parallel to their shorter axes (fig. SF11 in Supplementary File S1). We propose that the cleavage traces acted as weak planes and dictated the orientation of the transgranular fractures, which were subsequently invaded by hydrous fluids producing the narrow bands of symplectitised zones (Fig. 2c,d,i).

Although tectonic forces can produce brittle fractures, they can also originate in metamorphic rocks due to fluid overpressure (Pennacchioni 1996; Wawrzenitz et al. 2019) or reaction-induced volume change (Jamtveit et al. 2009). But the eclogite lacks evidence

supporting the latter, such as fluid-inclusion trails within the fractures (Pennacchioni 1996) and visible microchannels in high-contrast BSE images (Bukała et al. 2020). Therefore, we propose that the fractures in the omphacite grains originated due to tectonic stresses. The amphibole-plagioclase (\pm diopside) symplectite after omphacite in the studied eclogite was produced by omphacite + SiO₂ \rightarrow diopside + Na-plagioclase + H₂O \rightarrow (Na,Ca)-amphibole + Na-plagioclase (\pm diopside). The products diopside (density = 3.2 g cm⁻³), Na-plagioclase (2.6 g cm⁻³), and Na-Ca-amphibole (3.1 g cm⁻³) are less dense than the reactant omphacite (3.4 g cm⁻³) (Deer et al. 2013) and thus will occupy larger volumes than their parent. Hence, we believe it is unlikely that the volume increase associated with the symplectitisation had no role in omphacite fracturing.

Plagioclase and Amphibole

Plagioclase and amphibole CPO distributions demonstrate crystallographic inheritance from the parent omphacite, which is typical for symplectite complexes (McNamara et al. 2012; Heidelbach and Terry 2013; Rehman et al. 2016; Cao et al. 2020; Zertani et al. 2024; Chatterjee et al. 2024). For instance, in sample 17-6C, the following crystallographic relationships are observed between the product amphibole and parent omphacite crystals: $<001>_{Amp}//<001>_{Omp}$, $<010>_{Amp}//<010>_{Omp}$, and $<100>_{Amp}//<100>_{Omp}$ (Fig. 4c,d,g,h). These parallelisms are particularly demonstrated from Sites 1S and 1S-A (S1 symplectite) (Fig. 4c,d,g,h). Similar crystallographic relationships $(<0.10>_{Plag}//<0.01>_{Omp}$ and <001>Plag//<100>Omp) are also demonstrated between plagioclase and omphacite in Site 1S-A (Fig. 4h,i). Furthermore, the amphibole <100> and plagioclase <001> are oriented parallel to the long axes of the parent omphacite (Fig. 4c,d,g-i). At Site 2S (S2 symplectite), the expected crystallographic relationships between amphibole and plagioclase, such $<001>_{Amp}//<010>_{Plaq}$ and $<100>_{Amp}//<001>_{Plaq}$ (Fig. 4I,m), are also preserved. The orientations of the amphibole <100> and plagioclase <001>, in this case, probably indicate the long axis direction of the precursor omphacite.

Assuming tilt geometries for the subgrain boundaries, the plagioclase LAX distributions from Site 1S-A are roughly consistent with (010)<201> slip system activity, with minor contributions from (010)<001> and (-310)<001> slip systems (Fig. 6f). Of these, (010)<001> and (010)<201> have been previously reported as slip directions for plagioclase that deformed naturally by dislocation creep (Olsen and Kohlstedt 1984; Ji and Mainprice 1990; Kruse et al. 2001; Svahnberg and Piazolo 2010; Allard et al. 2021), Amphibole LAXs from Site 1S-A are preferentially distributed along the (100) with clusters parallel to the <010> (Fig. 6a), suggesting that intracrystalline deformation was dominantly accommodated by the (100)<001> slip system if we assume tilt subgrain boundaries (Lloyd et al. 1997). (100)<001> is the primary slip system for amphibole deformed via dislocation creep and has been widely reported in experimentally (Dollinger and Blacic 1975; Rooney et al. 1975; Morrison-Smith 1976; Ko and Jung 2015) as well as naturally deformed rocks (Skrotzki 1992; Berger and Stünitz 1996; Díaz Aspiroz et al. 2007; Cao et al. 2010; Elyaszadeh et al. 2018). For tilt boundaries, the dominance of (100)<001> cannot explain the cluster of intragrain misorientation axes parallel to the <001>. Such discordance, in the absence of evident microfracture or rigid body rotation in the symplectite amphibole, suggests that the subgrain boundaries are composed of both tilt and twist characteristics, and each LAX in the observed cluster parallel to the <001> resulted as the average of multiple misorientation axes associated with different slip systems (Lloyd 2004; Díaz Aspiroz et al. 2007).

Although amphibole and plagioclase LAXs from Site 2S are preferentially distributed along the (100) and (130), respectively, the correlated HAXs of amphibole (Fig. 6e) and plagioclase (Fig. 6i,j) are more randomly distributed in their respective crystal reference frames compared to those of Site 1S-A (Fig. 6a,f). One of the possibilities for such distributions could be that the symplectite constituents of Site 2S, unlike those of Site 1S-A, deformed in the presence of hydrous fluid by grain boundary sliding (Jiang et al. 2000; Svahnberg and Piazolo 2010; Fukuda and Okudaira 2013).

Crystal distortion and subgrain boundary development are also observed in the amphibole of the eclogite matrix (Fig. 8g–j). The LAXs for these amphibole grains cluster on the (001) and at low-angles to the <010>, implying glide of dislocations on either (001)<-100> or (100)<001> systems (Fig. 6f). Slip on the (001), however, would require the amphibole I-beam chains to break (Hacker and Christie 1990), and is reported only from single hornblende crystals deformed experimentally at ≤600°C (Morrison-Smith 1976). Therefore, (100)<001> is more likely to have been the active slip system.

Because of the largely continuous subgrain boundaries in the amphibole grains, we infer that 450°C marks the lower limit at which the grains deformed plastically (Biermann and Van Roermund 1983; Reynard et al. 1989). The amphibole in the symplectite complexes precipitated as direct replacements of the omphacite and diopside of the diopside-plagioclase symplectite in the presence of hydrous fluids. Because plagioclase crystallised before the invasion of fluids and amphibole crystallisation, it is likely that its deformation began under dry conditions and continued in the presence of hydrous fluid as the amphibole started to precipitate. However, the evidence at hand does not allow us to distinguish between the two. Dry plagioclase grains generally deform by brittle fracturing at low metamorphic grade conditions (<580 °C), whereas dislocation creep dominates at temperatures >600 °C (Olsen and Kohlstedt 1985; Kruse and Stünitz 1999; Altenberger and Wilhelm 2000; Kruse et al. 2001; Baratoux et al. 2005). Deformation experiments have demonstrated that wet anorthites and albites are weaker (Fukuda et al. 2022; Baïsset et al. 2024) and deform in the dislocation creep regime at temperatures at least ~150 °C lower than that of the dry aggregates (Tullis and Yund 1980; Rybacki and Dresen 2000, 2004). While making such comparisons, we must bear in mind that the 'dry' and 'wet' plagioclase used in the laboratory deformation experiments of Rybacki and Dresen (2000, 2004) contain <0.005 and ≥0.07 wt.% H₂O, respectively, whereas natural plagioclase from nominally anhydrous granulite rocks, e.g., Davenport Shear Zone in Australia, may contain up to 0.2 wt. % H₂O (Wex et al. 2018). Therefore, 'dry' plagioclase in naturally deformed rocks could most likely be as weak as the 'wet' plagioclase

used in the experiments of Rybacki and Dresen (2000, 2004). In naturally deformed plagioclase, dislocation creep activity has been observed at <500 °C (Shigematsu and Tanaka 2000). Also, natural amphibole-plagioclase aggregates can be 20–70% weaker with 1 wt% of added water (Hacker and Christie 1990). Therefore, plastic deformation and development of subgrain boundaries in the plagioclase grains in S1 symplectite (Fig. 8) continued as the eclogite exhumed to shallower depths corresponding to <10 kbar pressure.

Quartz

Quartz in the eclogite matrix consists of prominent subgrain boundaries (Figs. 2e,f, 12 k,l), which indicate that they deformed via dislocation creep (e.g., Hirth and Tullis, 1992; Vernon, 2018). Assuming tilt subgrain boundaries, the clustering of the LAXs parallel to the <0001> implies the dominance of {m}<a> slip system (Lloyd et al. 1997). Additional slip systems such as the {z}<a> and {r}<a> were also active because several other LAXs are parallel to the poles to (01-12) and (-1102), respectively (fig. SF8b in Supplementary File S1). Dey et al. (2022) have also reported {m}<a> slip system as the most common one from the quartz present in the matrix of retrograded and symplectite-bearing eclogites of the TMC from near the Kyagar Tso lake. These microstructural observations suggest deformation of the matrix guartz in the temperature range of 400 to <600 °C (Baëta and Ashbee 1969; Wilson 1975; Schmid and Casey 1986; Stipp et al. 2002), which is consistent with the temperatures predicted for the late-stage retrogression of the eclogite and metasedimentary rocks of the region in the amphibolite-greenschist facies conditions at <11 kbar (Guillot et al. 1997; Mukherjee et al. 2003). Assuming the water fugacity of wet quartzite, i.e., 5030 MPa (Tokle et al. 2019), the flow stresses of 13.5 MPa and 16.3 MPa, determined from the subgrain piezometer of (Goddard et al. 2020), when integrated into the flow laws of Hirth et al. (2001) and Tokle et al. (2019), predict strain rates in the range of 1.7×10^{-12} to 7.4×10^{-14} s⁻¹, which are comparable to geological strain rates.

Symplectite origin and evolution

Diopside-plagioclase symplectite (± amphibole ± quartz) is most commonly observed in the retrograded (U)HP eclogites (Joanny et al. 1991; Will and Schmädicke 2001; Štípská and Powell 2005; Groppo et al. 2007; Palmeri et al. 2009; Lanari et al. 2013; Renedo et al. 2015; Imayama et al. 2017; Dey et al. 2023; Zertani et al. 2024). Reports of symplectite with amphibole modal amounts greater than that of the coexisting diopsidic clinopyroxene are much fewer (Zhang et al. 2008; Scott et al. 2013; Liu et al. 2013; Martin 2019). Previous studies on eclogites containing amphibole-plagioclase symplectite reported that infiltration of water or water-rich fluid produced the amphibole that either replaced the omphacite (Liu et al. 2013; Tichomirowa and Köhler 2013) or the older diopsidic clinopyroxene in the symplectite at amphibolite facies conditions (Di Vincenzo and Palmeri 2001; Martin 2019). Although these studies did not characterise the source of the fluids, Martin (2019) argued that complete retrogression of omphacite into symplectite can only be achieved by an influx of external fluids. The author further added that the breakdown of peak-pressure hydrous minerals, such as phengite, during decompression can release fluids rich in hydrous components, which can facilitate amphibole crystallisation in the symplectite. However, because of the limited supply of such internally originated fluids, the replacement of omphacite grains by amphibole-bearing symplectite will be partial only. Although numerous relict omphacite grains, partially replaced by amphibole-plagioclase symplectite (S1) at their peripheries, persist in sample 17/6C (Fig. 2c,d), several precursor omphacite grains are wholly transformed into amphibole-plagioclase symplectite (S2) (Fig. 2j,k). Such disparities in the extents of symplectitisation suggest that time-integrated fluid influx was greater in the pockets dominated by S2 compared to those dominated by S1. The rate and extent of fluid influx also depend on how easily fluids can permeate through eclogites (Straume and Austrheim 1999; Konrad-Schmolke et al. 2011; Mindaleva et al. 2020). In sample 17/6C, the limited permeability of the eclogite could have restricted complete symplectitisation of the omphacite to only a few isolated pockets. We further observed that symplectitisation remained confined to the boundaries of omphacite

grains devoid of fractures (Fig. 2c,d). This suggests that both fluid availability and fracturing of the precursor omphacite grains acted together to produce completely symplectitised regions (S2) (Fig. 2j,k), which is illustrated sequentially in Fig. 10a–g. We have not observed textures indicative of the fluid being derived internally from phengite. But complete symplectitisation of omphacite and abundance of amphibole in the symplectites indicate that the fluid was of external origin. Externally sourced hydration of the Tso Morari eclogite at eclogite facies conditions and ~19 kbar has been proposed earlier (e.g., Palin et al. 2014) and more recently by Bidgood et al. (2024).

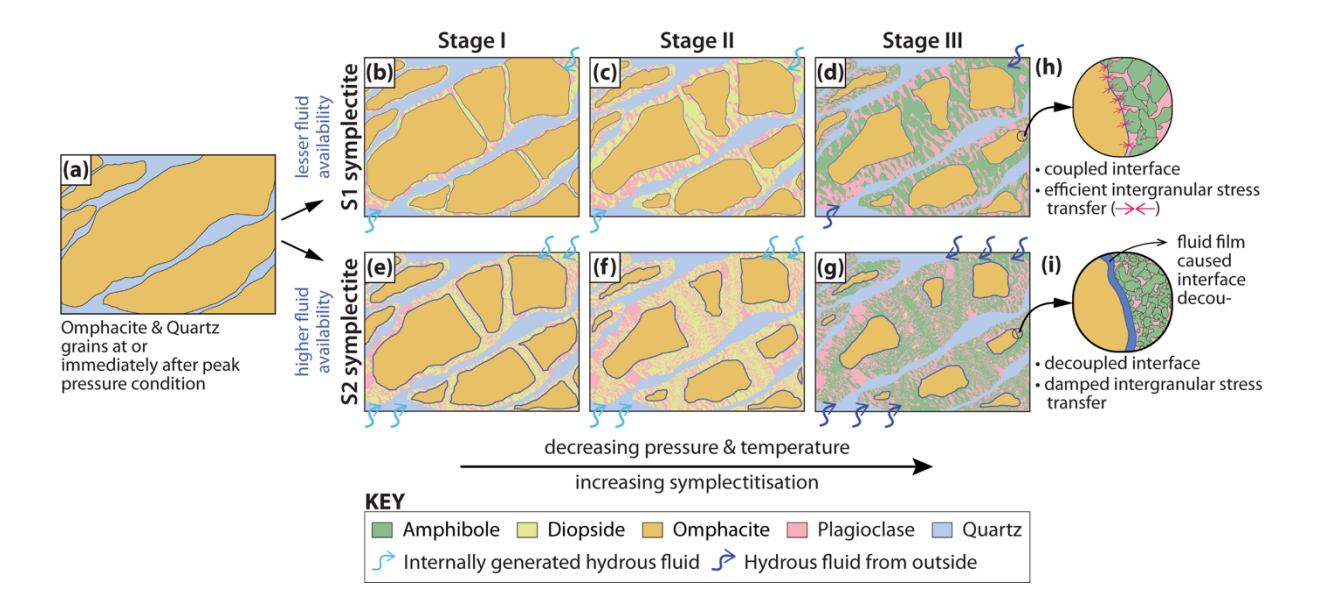


Fig. 10. Schematic figure illustrating the sequential development of the two categories of symplectite in the studied eclogite. (a) Omphacite and quartz assemblage in the eclogite at or immediately after peak pressure. Progressive symplectitisation and development of (b-d) S1 and (e-g) S2 symplectites. A greater supply of hydrous fluids generated more amphibole grains in the latter case. The relatively thinner peripheries of the omphacite grains in (b-d) than in (e-g) also represent the availability of more hydrous fluids in the latter. (h) and (i) show magnified illustrations of the omphacite-symplectite interfaces for the S1 and S2 symplectites, respectively. An additional Stage IV can be visualized for the S1 and S2 symplectites, characterized by the reduced size and disappearance, respectively, of the omphacite grains.

The Amp-S1 are relatively poorer in Si (6.78-7.24 apfu) than Amp-S2 (Si = 7.29-7.79 apfu) (Fig. 3b). The Amp-S2 (^TAl = 0.2-0.7 apfu) plot closer to the origin along the 1:1 line in the ^C(Al+Ti+Fe³⁺) + ^A(Na+K) v/s ^TAl correlation diagram than Amp-S1 (^TAl = 0.75-1.21 apfu) (Fig. 3d). These observations suggest sequential crystallisation of Amp-S2 after Amp-S1, with

progressive retrogression and symplectitisation. The amphibole grains of S1 symplectite have slight textural dissimilarities. Most of them are coarse and angular, whereas those closer to the omphacite boundaries are relatively finer and less angular in shape (fig. SF1c in Supplementary File S1). In the case of S2 symplectite, the finer amphibole grains are surrounded by the coarser ones (Fig. 2j,k). These textures suggest that omphacite replacement and symplectitisation progressed concentrically towards the cores of the grains. Consequently, the amphibole at the outermost rims crystallised earlier at relatively higher temperatures, with larger reaction overstep and rapid crystal growth due to faster ion diffusion, resulting in coarser grains. As retrogression progressed inward, sluggish diffusion at relatively lower temperatures produced numerous finer amphibole crystals instead (Boland and Van Roermund 1983; Joanny et al. 1991; Lanari et al. 2013). Such fluid-assisted concentric migration of sharp reaction fronts, facilitated by porosity creation due to the crystallisation of new phases, into less deformed older porphyroblasts, is common in exhumed eclogite facies rocks (Putnis and Austrheim 2010; Konrad-Schmolke et al. 2011). These features, along with the symplectitised fractures, support symplectitisation via dissolution-precipitation by the invading fluid (Putnis and Austrheim 2010; Spruzeniece et al. 2017).

The above processes also explain the gradual decrease in the grain sizes of amphibole constituting the symplectite, which occur as narrow bands across the omphacite, towards the remnant fragments of the omphacite (Fig. 2i,I). The linear nature of these symplectitic bands and parallel faces of the symplectite-omphacite interfaces on either side of the band suggest that symplectitisation progressed along omphacite fractures. The coarser amphibole grains (Fig. 2i,I) are arranged linearly, parallel to the shorter axis of the omphacite grain, and most likely represent the core of the fracture. Therefore, we infer that the microfractures in some omphacite grains were pivotal in facilitating their complete symplectitisation. It further confirms that the studied symplectite was porous, which allowed fluid to pass through and react with the pristine faces of the omphacite grains they mantled. Otherwise, the eclogite would have lacked both partially (Fig. 2i) and completely (Fig. 2j)

symplectitised omphacite grains. Our inferences, unlike those of Marti *et al.* (2018) and Zertani *et al.* (2024), agree with the experimental demonstrations of simultaneous increase in both porosity and volume during pseudomorphic replacements (Putnis et al. 2007; Xia et al. 2009).

Deformation of the garnet amphibolites

Amphibole

The strong CPOs of amphibole in the garnet amphibolite samples (Fig. 5c,g), along with the prominent subgrain boundaries (fig. SF9 in Supplementary File S1), support their intracrystalline deformation by the dislocation creep mechanism. The non-random distributions of their LAXs with respect to the crystallographic axes (fig. SF8c,f in Supplementary File S1) also confirm the same (Díaz Aspiroz et al. 2007). The distribution of amphibole LAXs of sample 20-2 shows a maximum that is nearly perpendicular to the (100) and (-100) with a sub-maximum parallel to the <001>. Assuming tilt subgrain boundaries, the former arrangement of LAXs could imply the dominance of either (010)<001> or (001)<010> slip systems. The cluster of LAXs parallel to <001> would imply activities of either (100)<010> or (010)<201> slip systems. In the case of sample 19-8B, the spread of amphibole LAXs along the (100) plane and the maxima parallel to the <001> suggest activities of either (100)<010> or (010)<100> slip systems. Amongst these, both (010)<001> and (010)<100> have been previously identified (Morrison-Smith 1976; Reynard et al. 1989; Skrotzki 1992; Díaz Aspiroz et al. 2007). (100)<010> is documented as a 'hard' slip system and difficult to trigger in naturally deformed amphibole (Elyaszadeh et al. 2018). Additionally, the clustering of amphibole intragrain misorientation axes around their <001> has been attributed to microfracturing and minute rigid body rotations (Soret et al. 2019; Jung et al. 2021). But since dislocation creep activity is prominent in the amphibole grains, we propose that the cluster of amphibole LAXs parallel to their c-axes resulted from the simultaneous operation of multiple slip systems (Díaz Aspiroz et al. 2007).

Although intracrystalline plastic deformation and subgrain formation in amphibole are essentially reported for temperatures above 600 °C (Skrotzki 1990, 1992; Berger and Stünitz 1996; Díaz Aspiroz et al. 2007; Cao et al. 2010), subgrains have been observed in amphibole grains deformed naturally in the temperature range 450–600 °C and <10–18 kbar pressure (Reynard et al. 1989). Therefore, we propose 450 °C as the minimum temperature at which the garnet amphibolites experienced plastic strain. At this temperature and geological strain rate of 10⁻¹⁴s⁻¹, the flow strength of garnet amphibolites (80% amphibole, 20% garnet) is estimated to be ~12 MPa (Wang et al. 2023).

The ^C(Al+Fe³⁺+Ti) + ^A(Na+K) and ^TAl contents of amphibole of the garnet amphibolite samples are higher than those of the symplectitic amphibole of sample 17-6C (Fig. 3d), implying that they equilibrated at higher temperatures than the latter (Nyman and Tracy 1993; Díaz Aspiroz et al. 2007; Cao et al. 2010). Furthermore, higher Al occupancy at the tetrahedral sites than the octahedral sites (fig. SF12 in Supplementary File S1) and lower Na occupancy at the B sites (Fig. 3c) (which is similar to those of the symplectitic amphibole grains) confirm their equilibration at low-pressure conditions (Brown 1977; Spear 1981, 1993; Palin et al. 2014).

Quartz

The quartz grains in both EBSD-mapped regions exhibit weak, nearly random CPOs (Fig. 5d,h) and lack subgrain boundaries. Although subgrains are present, they are limited to only a few coarse quartz grains in the thin sections (Figs 2e,f and 3b,f), whose sizes are comparable to the surrounding amphibole layers. These observations imply that quartz deformed at temperatures higher than 280 °C (Stipp et al. 2002), which caused some to develop strain-induced subgrains. Despite the lower dislocation creep flow strength of quartz compared to amphibole (Luan and Paterson 1992; Imon et al. 2004), pervasive subgrain development in quartz at higher temperatures could have been limited because the strain was partitioned into the thicker and monomineralic amphibole layers (e.g., Tatham et al., 2008).

Brodie and Rutter (1985) have postulated that despite being one of the strongest silicates, amphibole grains deform actively when present as the load-bearing framework.

Deformation v/s metamorphic reactions

Replacement reactions such as the ones producing symplectite are typically characterised by a reduction of bulk strength (reaction weakening) and grain sizes (Marti et al. 2018; Mansard et al. 2020; Zertani et al. 2024). Therefore, syn-metamorphic deformation of the reaction products progresses via grain-size sensitive creep mechanisms, viz. diffusion or dissolution-precipitation creep (McNamara et al. 2024; Zertani et al. 2024). Although rare, cases of grain-size insensitive or dislocation creep have been reported for symplectite (Odashima et al. 2007; Zhao et al. 2012; Doi et al. 2014). Dislocation creep-assisted intracrystalline deformation of the products of mineral transformation and replacement – particularly those that are inherently weaker, such as the plagioclase and amphibole, than their parents – can be triggered by the stress perturbations arising out of the volume increase resulting from the replacement reactions during retrogression (Greenwood and Johnson 1965; White and Knipe 1978; Poirier 1982, 1985; Brodie and Rutter 1985). Therefore, it is likely that despite their granular nature, the plagioclase and amphibole grains in the studied symplectite complexes deformed via dislocation creep.

We propose that the observed differences in the deformation mechanisms of plagioclase, which comprise the S1 and S2 symplectites, are due to the heterogeneous fluid distribution. Limited availability of hydrous fluid at Site 1S-A, coupled with increased stresses at the omphacite-symplectite interface (Fig. 10h), allowed the development of subgrain structures via dislocation activity in the weaker plagioclase grains even in the presence of the diopside grains (Greenwood and Johnson 1965; Kenkmann and Dresen 1998). The amphibole grains (Amp-S1) that replaced the diopsides later also deformed in the dislocation creep regime for the same reasons. Elevated stresses at the omphacite-symplectite interface also explain the subgrain boundaries in the plagioclase and amphibole grains adjacent to the

omphacite crystal in Site 1S-A (Figs 11a and 12a). In contrast, decoupling between the precursor omphacite and the S2 symplectite, due to the relatively higher supply of hydrous fluid (Fig. 10i), inhibited stress concentrations around the omphacite (Kenkmann and Dresen 1998) and, consequently, the plagioclase grains deformed via diffusion creep-accommodated grain boundary sliding, which randomised their HAXs (Fig. 6i,j) (Jiang et al. 2000; Svahnberg and Piazolo 2010). The randomly distributed HAXs (Fig. 6e) suggest that the amphibole grains of Site 2S also experienced grain boundary sliding, which was accommodated by dislocation motion instead and, consequently, produced the low-angle boundaries seen in the coarser crystals (Fig. 9d–f). Upon closer inspection, the amphibole grains in the symplectites appear to be dispersed in a plagioclase groundmass (fig. SF1 in Supplementary File S1). It is likely that plastic deformation of the amphibole grains, subsequent to the cessation of fluid ingress and symplectitisation, was dictated by the higher stresses they experienced compared to the weaker plagioclase groundmass (e.g., Hoover et al. 2022).

Conclusions

We investigated the deformation and mineralogical characteristics of the omphacite, amphibole-plagioclase symplectite, and the matrix components (amphibole and quartz) of an eclogite sample from the (U)HP Tso Morari region in the northwestern Indian Himalaya. We focused on the two varieties of symplectite, which replaced the omphacite grains partly along their peripheries (S1 symplectite) and completely (S2 symplectite). Albeit rare, fine diopside (Na = 0.18–0.25 apfu) is present in both S1 and S2, suggesting that amphibole replaced most of the precursor diopside. The omphacite grains (Na = 0.53–0.57 apfu) generally contain fractures, most of which are filled with symplectite. These fractures preferentially originated along the traces of the (100) cleavages due to tectonic stresses. The omphacite grains are chemically unzoned and devoid of subgrains, suggesting that they deformed via the body diffusion creep. The absence of subgrains in omphacite also suggests that flow stresses were

below 16 MPa at peak thermal conditions. The omphacite CPOs are inherited by amphibole and plagioclase, constituting the symplectites such that <001>_{Omp}//<001>_{Amp}//<010>_{Plag}, $<0.10>_{Omp}//<0.10>_{Amp}$, and $<1.00>_{Omp}//<1.00>_{Amp}//<0.01>_{Plag}$. The amphibole grains in S1 (Amph-S1) are poorer in Si (6.75-7.34 apfu) compared to those in S2 (Amph-S2; Si = 7.29-7.79 apfu), indicating that the latter crystallised at lower temperatures than the former during retrogression. The heterogeneous distribution of the hydrous fluid, because of the heterogeneous permeability in the eclogite, was responsible for the varied degrees of symplectitisation. Relatively lower fluid supplies to S1 and elevated stresses at the omphacite-symplectite interface allowed the plagioclase grains to deform via dislocation activity, with (010)<201> and (010)<001> as the probable slip systems. In contrast, due to greater fluid availability, the plagioclase in S2 deformed via diffusion creep-accommodated grain boundary sliding. Subgrain walls, with misorientations (4–9°) comparable to those observed in the amphibole grains of the eclogite matrix and garnet amphibolites, are present in some of the coarser Amp-S1 and Amp-S2, suggesting dislocation activity. The LAX distribution of Amp-S1 is consistent with the known (100)<001> slip system for amphibole, which is also predicted for those in the eclogite matrix. In contrast, Amp-S2 deformed via grain boundary sliding, accommodated by dislocation creep. These characteristics suggest that plastic deformation of the amphibole grains continued till the eclogite and garnet amphibolites reached depths corresponding to <10 kbar pressure, which also agrees with the lower Na occupancies (<1.0 apfu) at their Bsites. Subgrain size piezometry employed on a coarse quartz grain from the eclogite matrix estimated a paleostress of ~16 MPa.

Data availability

The EBSD data used in this study can be accessed from Zenodo Data Repository (https://doi.org/10.5281/zenodo.14776239). Representative mineral chemistry data are provided in the Electronic Supplementary Material file S1.

Acknowledgements

This work is funded by the Grant-in-Aid for JSPS Fellows (23KF0120) and Grant-in-Aid Scientific Research (23K22595) awarded by the Japan Society for the Promotion of Science (JSPS). The authors thank Prof. Andrew Smye for editorial handling and Prof. Brendan Dyck for thoroughly reviewing the manuscript. Comments by the Editor-in-Chief Prof. Othmar Müntener are also appreciated. Their suggestions improved the manuscript considerably.

Author contributions

Dripta Dutta: Conceptualization, Data Curation, Formal Analysis, Funding acquisition, Investigation, Methodology, Project administration, Validation, Visualization, Writing – original draft, Writing – review & editing; **Takeshi Imayama**: Conceptualization, Funding acquisition, Investigation, Methodology, Project administration, Resources, Validation, Writing – review & editing; **Dyuti Prakash Sarkar**: Data Curation, Methodology, Validation, Writing – review & editing; **Jun-ichi Ando**: Methodology, Validation, Resources, Writing – review & editing; **Kaushik Das**: Methodology, Validation, Resources, Writing – review & editing.

References

- Ahmad T, Bhat IM, Tanaka T, et al (2022) Tso Morari Eclogites, Eastern Ladakh: Isotopic and Elemental Constraints on Their Protolith, Genesis, and Tectonic Setting. J Geol 130:231–252. https://doi.org/10.1086/719333
- Allard M, Ildefonse B, Oliot É, Barou F (2021) Plastic Deformation of Plagioclase in Oceanic Gabbro Accreted at a Slow-Spreading Ridge (Hole U1473A, Atlantis Bank, Southwest Indian Ridge). J Geophys Res Solid Earth 126:. https://doi.org/10.1029/2021JB021964
- Altenberger U, Wilhelm S (2000) Ductile deformation of K-feldspar in dry eclogite facies shear zones in the Bergen Arcs, Norway. Tectonophysics 320:107–121. https://doi.org/10.1016/S0040-1951(00)00048-2

- Bachmann F, Hielscher R, Schaeben H (2011) Grain detection from 2d and 3d EBSD data— Specification of the MTEX algorithm. Ultramicroscopy 111:1720–1733. https://doi.org/10.1016/j.ultramic.2011.08.002
- Baëta RD, Ashbee KHG (1969) Slip systems in quartz: I. Experiments. Am Mineral 54:1551–1573
- Baïsset M, Labrousse L, Schubnel A, et al (2024) Rheology of hydrated plagioclase at lower crustal conditions: Cataclasis, creep and transformational plasticity. J Struct Geol 178:105010. https://doi.org/10.1016/j.jsg.2023.105010
- Baratoux L, Schulmann K, Ulrich S, Lexa O (2005) Contrasting microstructures and deformation mechanisms in metagabbro mylonites contemporaneously deformed under different temperatures (c. 650 °C and c. 750 °C). In: Gapais D, Brun JP, Cobbold PR (eds) Deformation Mechanisms, Rheology and Tectonics: from Minerals to the Lithosphere. Geological Society of London Special Publications. pp 97–125
- Barker AJ (1998) Mineral inclusions, intergrowths and coronas. In: Introduction to Metamorphic Textures and Microstructures. Stanley Thomes (Publishers) Ltd, Cheltenham, United Kingdom, pp 85–100
- Berger A, Stünitz H (1996) Deformation mechanisms and reaction of hornblende: examples from the Bergell tonalite (Central Alps). Tectonophysics 257:149–174. https://doi.org/10.1016/0040-1951(95)00125-5
- Bidgood AK, Parsons AJ, Roberts NMW, et al (2024) The Geodynamic Significance of Continental UHP Exhumation: New Constraints From the Tso Morari Complex, NW Himalaya. Tectonics 43:e2023TC007976. https://doi.org/10.1029/2023TC007976
- Biermann C, Van Roermund HLM (1983) Defect structures in naturally deformed clinoamphiboles—a TEM study. Tectonophysics 95:267–278. https://doi.org/10.1016/0040-1951(83)90072-0
- Boland JN, Van Roermund HLM (1983) Mechanisms of exsolution in omphacites from high temperature, type B, eclogites. Phys Chem Miner 9:30–37. https://doi.org/10.1007/BF00309467
- Brenker FE, Prior DJ, Müller WF (2002) Cation ordering in omphacite and effect on deformation mechanism and lattice preferred orientation (LPO). J Struct Geol 24:1991–2005. https://doi.org/10.1016/S0191-8141(02)00010-X
- Brodie KH (1995) The development of orientated symplectites during deformation. J Metamorph Geol 13:499–508. https://doi.org/10.1111/j.1525-1314.1995.tb00237.x
- Brodie KH, Rutter EH (1987) The role of transiently fine-grained reaction products in syntectonic metamorphism: natural and experimental examples. Can J Earth Sci 24:556–564. https://doi.org/10.1139/e87-054
- Brodie KH, Rutter EH (1985) On the Relationship between Deformation and Metamorphism, with Special Reference to the Behavior of Basic Rocks. In: Thompson AB, Rubie DC (eds) Metamorphic Reactions. Springer New York, New York, NY, pp 138–179
- Brown EH (1977) The Crossite Content of Ca-Amphibole as a Guide to Pressure of Metamorphism. J Petrol 18:53–72. https://doi.org/10.1093/petrology/18.1.53

- Buchs N, Epard J-L (2019) Geology of the eastern part of the Tso Morari nappe, the Nidar Ophiolite and the surrounding tectonic units (NW Himalaya, India). J Maps 15:38–48. https://doi.org/10.1080/17445647.2018.1541196
- Bukała M, Barnes CJ, Jeanneret P, et al (2020) Brittle Deformation During Eclogitization of Early Paleozoic Blueschist. Front Earth Sci 8:. https://doi.org/10.3389/feart.2020.594453
- Cao S, Liu J, Leiss B (2010) Orientation-related deformation mechanisms of naturally deformed amphibole in amphibolite mylonites from the Diancang Shan, SW Yunnan, China. J Struct Geol 32:606–622. https://doi.org/10.1016/j.jsg.2010.03.012
- Cao Y, Du J, Park M, et al (2020) Metastability and Nondislocation-Based Deformation Mechanisms of the Flem Eclogite in the Western Gneiss Region, Norway. J Geophys Res Solid Earth 125:e2020JB019375. https://doi.org/10.1029/2020JB019375
- Chatterjee A, Daczko NR, Dey J, Piazolo S (2024) Hydrous shear zones are sites of melt transfer in the lower arc crust: A case study from Fiordland, New Zealand. J Metamorph Geol 42:933–956. https://doi.org/10.1111/jmg.12788
- Chatterjee N, Jagoutz O (2015) Exhumation of the UHP Tso Morari eclogite as a diapir rising through the mantle wedge. Contrib Mineral Petrol 169:3. https://doi.org/10.1007/s00410-014-1099-y
- Crameri F (2018) Scientific colour maps. Zenodo. http://doi.org/10.5281/zenodo.1243862
- de Sigoyer J, Guillot S, Dick P (2004) Exhumation of the ultrahigh-pressure Tso Morari unit in eastern Ladakh (NW Himalaya): A case study. Tectonics 23:1–18. https://doi.org/10.1029/2002TC001492
- de Sigoyer J, Guillot S, Lardeaux J-M, Mascle G (1997) Glaucophane-bearing eclogites in the Tso Morari dome (eastern Ladakh, NW Himalaya). Eur J Mineral 9:1073–1084. https://doi.org/10.1127/ejm/9/5/1073
- Deer WA, Howie RA, Zussman J (2013) An Introduction to the Rock-Forming Minerals, Third. Mineralogical Society of Great Britain and Ireland, UK
- Dey A, Sen K, Mamtani MA (2022) Electron Backscatter Diffraction Study of Ultrahigh-Pressure Tso Morari Eclogites (Trans-Himalayan Collisional Zone): Implications for Strain Regime Transition from Constrictional to Plane Strain during Exhumation. Lithosphere 2022:7256746. https://doi.org/10.2113/2022/7256746
- Dey A, Sen K, Sen A, Choudhary S (2023) Omphacite breakdown, symplectite formation and carbonate metasomatism in a retrograded continental eclogite: Implications for the exhumation of the Tso Morari Crystalline Complex (Trans-Himalaya, NW India). Phys Chem Earth Parts ABC 131:103453. https://doi.org/10.1016/j.pce.2023.103453
- Di Vincenzo G, Palmeri R (2001) An 40Ar–39Ar investigation of high-pressure metamorphism and the retrogressive history of mafic eclogites from the Lanterman Range (Antarctica): evidence against a simple temperature control on argon transport in amphibole. Contrib Mineral Petrol 141:15–35. https://doi.org/10.1007/s004100000226
- Díaz Aspiroz M, Lloyd GE, Fernández C (2007) Development of lattice preferred orientation in clinoamphiboles deformed under low-pressure metamorphic conditions. A

- SEM/EBSD study of metabasites from the Aracena metamorphic belt (SW Spain). J Struct Geol 29:629–645. https://doi.org/10.1016/j.jsg.2006.10.010
- Dimanov A, Dresen G (2005) Rheology of synthetic anorthite-diopside aggregates: Implications for ductile shear zones. J Geophys Res Solid Earth 110:. https://doi.org/10.1029/2004JB003431
- Doi N, Kato T, Kubo T, et al (2014) Creep behavior during the eutectoid transformation of albite: Implications for the slab deformation in the lower mantle. Earth Planet Sci Lett 388:92–97. https://doi.org/10.1016/j.epsl.2013.09.009
- Dollinger G, Blacic JD (1975) Deformation mechanisms in experimentally and naturally deformed amphiboles. Earth Planet Sci Lett 26:409–416. https://doi.org/10.1016/0012-821X(75)90016-3
- Droop GTR (1987) A general equation for estimating Fe3+ concentrations in ferromagnesian silicates and oxides from microprobe analyses, using stoichiometric criteria. Mineral Mag 51:431–435. https://doi.org/10.1180/minmag.1987.051.361.10
- Duretz T, Gerya TV (2013) Slab detachment during continental collision: Influence of crustal rheology and interaction with lithospheric delamination. Tectonophysics 602:124–140. https://doi.org/10.1016/j.tecto.2012.12.024
- Dutta D, Misra S, Karmakar S (2022) Deformation mechanisms and characteristics of the meta-BIFs from an early Proterozoic shear system of the Southern Granulite Terrane (SGT), India. J Struct Geol 156:104534. https://doi.org/10.1016/j.jsg.2022.104534
- Dutta D, Mukherjee S (2021) Extrusion kinematics of UHP terrane in a collisional orogen: EBSD and microstructure-based approach from the Tso Morari Crystallines (Ladakh Himalaya). Tectonophysics 800:228641. https://doi.org/10.1016/j.tecto.2020.228641
- Elyaszadeh R, Prior DJ, Sarkarinejad K, Mansouri H (2018) Different slip systems controlling crystallographic preferred orientation and intracrystalline deformation of amphibole in mylonites from the Neyriz mantle diapir, Iran. J Struct Geol 107:38–52. https://doi.org/10.1016/j.jsg.2017.11.020
- Epard J-L, Steck A (2008) Structural development of the Tso Morari ultra-high pressure nappe of the Ladakh Himalaya. Tectonophysics 451:242–264. https://doi.org/10.1016/j.tecto.2007.11.050
- Fukuda J, Muto J, Koizumi S, et al (2022) Enhancement of ductile deformation in polycrystalline anorthite due to the addition of water. J Struct Geol 156:104547. https://doi.org/10.1016/j.jsg.2022.104547
- Fukuda J, Okudaira T (2013) Grain-size-sensitive creep of plagioclase accompanied by solution–precipitation and mass transfer under mid-crustal conditions. J Struct Geol 51:61–73. https://doi.org/10.1016/j.jsg.2013.03.006
- Gaidies F, Milke R, Heinrich W, Abart R (2017) Metamorphic mineral reactions:
 Porphyroblast, corona and symplectite growth. In: Heinrich W, Abart R (eds) Mineral reaction kinetics: Microstructures, textures, chemical and isotopic signatures.
 European Mineralogical Union and Mineralogical Society of Great Britain and Ireland, p 0

- García-Casco A, Torres-Roldán RL (1996) Disequilibrium Induced by Fast Decompression in St–Bt–Grt–Ky–Sil–And Metapelites from the Betic Belt (Southern Spain). J Petrol 37:1207–1239. https://doi.org/10.1093/petrology/37.5.1207
- Gerya TV, Stöckhert B, Perchuk AL (2002) Exhumation of high-pressure metamorphic rocks in a subduction channel: A numerical simulation: EXHUMATION OF HIGH-PRESSURE ROCKS. Tectonics 21:6-1-6–19. https://doi.org/10.1029/2002TC001406
- Godard G, Van Roermund HLM (1995) Deformation-induced clinopyroxene fabrics from eclogites. J Struct Geol 17:1425–1443. https://doi.org/10.1016/0191-8141(95)00038-F
- Goddard RM, Hansen LN, Wallis D, et al (2020) A Subgrain-Size Piezometer Calibrated for EBSD. Geophys Res Lett 47:e2020GL090056. https://doi.org/10.1029/2020GL090056
- Greenwood GW, Johnson RH (1965) The deformation of metals under small stresses during phase transformations. Proc R Soc Lond Ser Math Phys Sci 283:403–422. https://doi.org/10.1098/rspa.1965.0029
- Groppo C, Lombardo B, Castelli D, Compagnoni R (2007) Exhumation History of the UHPM Brossasco-Isasca Unit, Dora-Maira Massif, as Inferred from a Phengite-Amphibole Eclogite. Int Geol Rev 49:142–168. https://doi.org/10.2747/0020-6814.49.2.142
- Guillot S, de Sigoyer J, Lardeaux JM, Mascle G (1997) Eclogitic metasediments from the Tso Morari area (Ladakh, Himalaya): evidence for continental subduction during India-Asia convergence. Contrib Mineral Petrol 128:197–212. https://doi.org/10.1007/s004100050303
- Guillot S, Hattori KH, de Sigoyer J, et al (2001) Evidence of hydration of the mantle wedge and its role in the exhumation of eclogites. Earth Planet Sci Lett 193:115–127. https://doi.org/10.1016/S0012-821X(01)00490-3
- Hacker BR, Christie JM (1990) Brittle/Ductile and Plastic/Cataclastic Transitions in Experimentally Deformed and Metamorphosed Amphibolite. In: Duba AG, Durham WB, Handin JW, Wang HF (eds) The Brittle-Ductile Transition in Rocks. American Geophysical Union (AGU), pp 127–147
- Hawthorne FC, Oberti R, Harlow GE, et al (2012) Nomenclature of the amphibole supergroup. Am Mineral 97:2031–2048. https://doi.org/10.2138/am.2012.4276
- Heidelbach F, Terry MP (2013) Inherited Fabric in an Omphacite Symplectite: Reconstruction of Plastic Deformation under Ultra-High Pressure Conditions. Microsc Microanal 19:942–949. https://doi.org/10.1017/S1431927613001451
- Hermann J, Rubatto D, Korsakov A, Shatsky VS (2001) Multiple zircon growth during fast exhumation of diamondiferous, deeply subducted continental crust (Kokchetav Massif, Kazakhstan). Contrib Mineral Petrol 141:66–82. https://doi.org/10.1007/s004100000218
- Hess BL, Ague JJ (2024) Orientation Piezometry: Methods for Quantifying Stress From the Compositions and Orientations of Multicomponent Minerals. J Geophys Res Solid Earth 129:e2024JB030113. https://doi.org/10.1029/2024JB030113

- Hielscher R, Schaeben H (2008) A novel pole figure inversion method: specification of the *MTEX* algorithm. J Appl Crystallogr 41:1024–1037. https://doi.org/10.1107/S0021889808030112
- Hirth G, Teyssier C, Dunlap JW (2001) An evaluation of quartzite flow laws based on comparisons between experimentally and naturally deformed rocks. Int J Earth Sci 90:77–87. https://doi.org/10.1007/s005310000152
- Hirth G, Tullis J (1992) Dislocation creep regimes in quartz aggregates. J Struct Geol 14:145–159. https://doi.org/10.1016/0191-8141(92)90053-Y
- Holyoke CW, Kronenberg AK (2010) Accurate differential stress measurement using the molten salt cell and solid salt assemblies in the Griggs apparatus with applications to strength, piezometers and rheology. Tectonophysics 494:17–31. https://doi.org/10.1016/j.tecto.2010.08.001
- Hoover WF, Condit CB, Lindquist PC, et al (2022) Episodic Slow Slip Hosted by Talc-Bearing Metasomatic Rocks: High Strain Rates and Stress Amplification in a Chemically Reacting Shear Zone. Geophys Res Lett 49:e2022GL101083. https://doi.org/10.1029/2022GL101083
- Imayama T, Dutta D, Yi K (2024) The origin of the ultrahigh-pressure Tso Morari complex, NW Himalaya: implication for early Paleozoic rifting. Geol Mag 1–8. https://doi.org/10.1017/S0016756824000025
- Imayama T, Oh C-W, Baltybaev SK, et al (2017) Paleoproterozoic high-pressure metamorphic history of the Salma eclogite on the Kola Peninsula, Russia. Lithosphere 9:855–873. https://doi.org/10.1130/L657.1
- Imon R, Okudaira T, Kanagawa K (2004) Development of shape- and lattice-preferred orientations of amphibole grains during initial cataclastic deformation and subsequent deformation by dissolution-precipitation creep in amphibolites from the Ryoke metamorphic belt, SW Japan. J Struct Geol 26:793–805. https://doi.org/10.1016/j.jsg.2003.09.004
- Jamtveit B, Austrheim H, Putnis A (2016) Disequilibrium metamorphism of stressed lithosphere. Earth-Sci Rev 154:1–13. https://doi.org/10.1016/j.earscirev.2015.12.002
- Jamtveit B, Putnis CV, Malthe-Sørenssen A (2009) Reaction induced fracturing during replacement processes. Contrib Mineral Petrol 157:127–133. https://doi.org/10.1007/s00410-008-0324-y
- Ji S, Mainprice D (1990) Recrystallization and Fabric Development in Plagioclase. J Geol 98:65–79
- Jiang Z, Prior DJ, Wheeler J (2000) Albite crystallographic preferred orientation and grain misorientation distribution in a low-grade mylonite: implications for granular flow. J Struct Geol 22:1663–1674. https://doi.org/10.1016/S0191-8141(00)00079-1
- Joanny V, Van Roermund H, Lardeaux JM (1991) The clinopyroxene/plagioclase symplectite in retrograde eclogites: A potential geothermobarometer. Geol Rundsch 80:303–320. https://doi.org/10.1007/BF01829368
- Jonnalagadda MK, Karmalkar NR, Duraiswami RA (2019) Geochemistry of eclogites of the Tso Morari complex, Ladakh, NW Himalayas: Insights into trace element behavior

- during subduction and exhumation. Geosci Front 10:811–826. https://doi.org/10.1016/j.gsf.2017.05.013
- Jung S, Yamamoto T, Ando J, Jung H (2021) Dislocation Creep of Olivine and Amphibole in Amphibole Peridotites from Åheim, Norway. Minerals 11:1018. https://doi.org/10.3390/min11091018
- Kenkmann T, Dresen G (1998) Stress gradients around porphyroclasts: palaeopiezometric estimates and numerical modelling. J Struct Geol 20:163–173. https://doi.org/10.1016/S0191-8141(97)00074-6
- Ko B, Jung H (2015) Crystal preferred orientation of an amphibole experimentally deformed by simple shear. Nat Commun 6:6586. https://doi.org/10.1038/ncomms7586
- Konrad-Schmolke M, O'Brien PJ, Zack T (2011) Fluid Migration above a Subducted Slab—Constraints on Amount, Pathways and Major Element Mobility from Partially Overprinted Eclogite-facies Rocks (Sesia Zone, Western Alps). J Petrol 52:457–486. https://doi.org/10.1093/petrology/egg087
- Kruse R, Stünitz H (1999) Deformation mechanisms and phase distribution in mafic high-temperature mylonites from the Jotun Nappe, southern Norway. Tectonophysics 303:223–249. https://doi.org/10.1016/S0040-1951(98)00255-8
- Kruse R, Stünitz H, Kunze K (2001) Dynamic recrystallization processes in plagioclase porphyroclasts. J Struct Geol 23:1781–1802. https://doi.org/10.1016/S0191-8141(01)00030-X
- Kylander-Clark ARC, Hacker BR, Mattinson CG (2012) Size and exhumation rate of ultrahigh-pressure terranes linked to orogenic stage. Earth Planet Sci Lett 321–322:115–120. https://doi.org/10.1016/j.epsl.2011.12.036
- Lanari P, Riel N, Guillot S, et al (2013) Deciphering high-pressure metamorphism in collisional context using microprobe mapping methods: Application to the Stak eclogitic massif (northwest Himalaya). Geology 41:111–114. https://doi.org/10.1130/G33523.1
- Leake BE, Woolley AR, Arps CES, et al (1997) Nomenclature of amphiboles; report of the subcommittee on amphiboles of the International Mineralogical Association, Commission on New Minerals and Mineral Names. Can Mineral 35:219–246
- Liu Q, Hermann J, Zhang J (2013) Polyphase inclusions in the Shuanghe UHP eclogites formed by subsolidus transformation and incipient melting during exhumation of deeply subducted crust. Lithos 177:91–109. https://doi.org/10.1016/j.lithos.2013.06.010
- Lloyd GE (2004) Microstructural evolution in a mylonitic quartz simple shear zone: the significant roles of dauphine twinning and misorientation. Flow Process Faults Shear Zones Geol Soc Lond Spec Publ 224:39–61. https://doi.org/10.1144/GSL.SP.2004.224.01.04
- Lloyd GE, Farmer AB, Mainprice D (1997) Misorientation analysis and the formation and orientation of subgrain and grain boundaries. Tectonophysics 279:55–78. https://doi.org/10.1016/S0040-1951(97)00115-7

- Long SP, Kohn MJ, Kerswell BC, et al (2020) Thermometry and Microstructural Analysis Imply Protracted Extensional Exhumation of the Tso Morari UHP Nappe, Northwestern Himalaya: Implications for Models of UHP Exhumation. Tectonics 39:e2020TC006482. https://doi.org/10.1029/2020TC006482
- Luan FC, Paterson MS (1992) Preparation and deformation of synthetic aggregates of quartz. J Geophys Res Solid Earth 97:301–320. https://doi.org/10.1029/91JB01748
- Mansard N, Stünitz H, Raimbourg H, et al (2020) Relationship between microstructures and resistance in mafic assemblages that deform and transform. Solid Earth 11:2141–2167. https://doi.org/10.5194/se-11-2141-2020
- Marti S, Stünitz H, Heilbronner R, et al (2018) Syn-kinematic hydration reactions, grain size reduction, and dissolution–precipitation creep in experimentally deformed plagioclase–pyroxene mixtures. Solid Earth 9:985–1009. https://doi.org/10.5194/se-9-985-2018
- Martin C (2019) P-T conditions of symplectite formation in the eclogites from the Western Gneiss Region (Norway). In: Ferrero S, Lanari P, Goncalves P, Grosch EG (eds) Metamorphic Geology: Microscale to Mountain Belts. Geological Society of London Special Publications. pp 197–216
- Martin C, Duchêne S (2015) Residual water in hydrous minerals as a kinetic factor for omphacite destabilization into symplectite in the eclogites of Vårdalsneset (WGR, Norway). Lithos 232:162–173. https://doi.org/10.1016/j.lithos.2015.06.021
- Massonne H-J (2012) Formation of Amphibole and Clinozoisite–Epidote in Eclogite owing to Fluid Infiltration during Exhumation in a Subduction Channel. J Petrol 53:1969–1998. https://doi.org/10.1093/petrology/egs040
- Mauler A, Godard G, Kunze K (2001) Crystallographic fabrics of omphacite, rutile and quartz in Vendée eclogites (Armorican Massif, France). Consequences for deformation mechanisms and regimes. Tectonophysics 342:81–112. https://doi.org/10.1016/S0040-1951(01)00157-3
- McNamara DD, Wheeler J, Pearce M, Prior DJ (2012) Fabrics produced mimetically during static metamorphism in retrogressed eclogites from the Zermatt-Saas zone, Western Italian Alps. J Struct Geol 44:167–178. https://doi.org/10.1016/j.jsg.2012.08.006
- McNamara DD, Wheeler J, Pearce M, Prior DJ (2024) A key role for diffusion creep in eclogites: Omphacite deformation in the Zermatt-Saas unit, Italian Alps. J Struct Geol 179:105033. https://doi.org/10.1016/j.jsg.2023.105033
- Mindaleva D, Uno M, Higashino F, et al (2020) Rapid fluid infiltration and permeability enhancement during middle–lower crustal fracturing: Evidence from amphibolite–granulite-facies fluid–rock reaction zones, Sør Rondane Mountains, East Antarctica. Lithos 372–373:105521. https://doi.org/10.1016/j.lithos.2020.105521
- Morimoto N (1989) Nomenclature of pyroxenes. Mineral J 14:198–221. https://doi.org/10.2465/minerj.14.198
- Mørk MBE (1985) Incomplete high P–T metamorphic transitions within the Kvamsøy pyroxenite complex, west Norway: a case study of disequilibrium. J Metamorph Geol 3:245–264. https://doi.org/10.1111/i.1525-1314.1985.tb00320.x

- Morrison-Smith DJ (1976) Transmission electron microscopy of experimentally deformed hornblende. Am Mineral 61:272–280
- Mukherjee BK, Sachan HK, Ogasawara Y, et al (2003) Carbonate-Bearing UHPM Rocks from the Tso-Morari Region, Ladakh, India: Petrological Implications. Int Geol Rev 45:49–69. https://doi.org/10.2747/0020-6814.45.1.49
- Nyman MW, Tracy RJ (1993) Petrological evolution of amphibolite shear zones, Cheyenne Belt, south-eastern Wyoming, USA. J Metamorph Geol 11:757–773. https://doi.org/10.1111/j.1525-1314.1993.tb00185.x
- O'Brien PJ (1993) Partially retrograded eclogites of the Münchberg Massif, Germany: records of a multi-stage Variscan uplift history in the Bohemian Massif. J Metamorph Geol 11:241–260. https://doi.org/10.1111/j.1525-1314.1993.tb00145.x
- Odashima N, Morishita T, Ozawa K, et al (2007) Formation and deformation mechanisms of pyroxene-spinel symplectite in an ascending mantle, the Horoman peridotite complex, Japan: An EBSD (electron backscatter diffraction) study. J Mineral Petrol Sci 103:1–15. https://doi.org/10.2465/jmps.070222b
- Ogilvie P, Gibson RL (2017) Arrested development a comparative analysis of multilayer corona textures in high-grade metamorphic rocks. Solid Earth 8:93–135. https://doi.org/10.5194/se-8-93-2017
- Olsen TS, Kohlstedt DL (1984) Analysis of dislocations in some naturally deformed plagioclase feldspars. Phys Chem Miner 11:153–160. https://doi.org/10.1007/BF00387845
- Olsen TS, Kohlstedt DL (1985) Natural deformation and recrystallization of some intermediate plagioclase feldspars. Tectonophysics 111:107–131. https://doi.org/10.1016/0040-1951(85)90067-8
- Palin RM, St-Onge MR, Waters DJ, et al (2014) Phase equilibria modelling of retrograde amphibole and clinozoisite in mafic eclogite from the Tso Morari massif, northwest India: constraining the *P T M* (H ₂ O) conditions of exhumation. J Metamorph Geol 32:675–693. https://doi.org/10.1111/jmg.12085
- Palmeri R, Chmielowski R, Sandroni S, et al (2009) Petrology of the eclogites from western Tasmania: Insights into the Cambro-Ordovician evolution of the paleo-Pacific margin of Gondwana. Lithos 109:223–239. https://doi.org/10.1016/j.lithos.2008.06.016
- Parrish RR, Gough SJ, Searle MP, Waters DJ (2006) Plate velocity exhumation of ultrahigh-pressure eclogites in the Pakistan Himalaya. Geology 34:989. https://doi.org/10.1130/G22796A.1
- Paterson MS, Wong T (eds) (2005) Experimental Studies on the Brittle Fracture Stress. In: Experimental Rock Deformation The Brittle Field. Springer, Berlin, Heidelberg, pp 17–44
- Pennacchioni G (1996) Progressive eclogitization under fluid-present conditions of pre-Alpine mafic granulites in the Austroalpine Mt Emilius Klippe (Italian Western Alps). J Struct Geol 18:549–561. https://doi.org/10.1016/S0191-8141(96)80023-X

- Peterman EM, Grove M (2010) Growth conditions of symplectic muscovite + quartz: Implications for quantifying retrograde metamorphism in exhumed magmatic arcs. Geology 38:1071–1074. https://doi.org/10.1130/G31449.1
- Poirier JP (1982) On transformation plasticity. J Geophys Res Solid Earth 87:6791–6797. https://doi.org/10.1029/JB087iB08p06791
- Poirier J-P (ed) (1985) Transformation plasticity. In: Creep of Crystals: High-Temperature Deformation Processes in Metals, Ceramics and Minerals. Cambridge University Press, Cambridge, pp 213–228
- Putnis A, Austrheim H (2010) Fluid-induced processes: metasomatism and metamorphism. Geofluids 10:254–269. https://doi.org/10.1111/j.1468-8123.2010.00285.x
- Putnis CV, Geisler T, Schmid-Beurmann P, et al (2007) An experimental study of the replacement of leucite by analcime. Am Mineral 92:19–26. https://doi.org/10.2138/am.2007.2249
- Rehman HU, Mainprice D, Barou F, et al (2016) EBSD-measured crystal preferred orientation of eclogites from the Sanbagawa metamorphic belt, central Shikoku, SW Japan. Eur J Mineral 28:1155–1168. https://doi.org/10.1127/ejm/2016/0028-2574
- Renedo RN, Nachlas WO, Whitney DL, et al (2015) Fabric development during exhumation from ultrahigh-pressure in an eclogite-bearing shear zone, Western Gneiss Region, Norway. J Struct Geol 71:58–70. https://doi.org/10.1016/j.jsg.2014.09.012
- Reynard B, Gillet P, Willaime C (1989) Deformation mechanisms in naturally deformed glaucophanes; a TEM and HREM study. Eur J Mineral 1:611–624
- Robinson P, Ross M, Jaefe HW (1971) Composition of the Anthophyllite-Gedrite Series, Comparisons of Gedrite and Hornblende, and the Anthophyllite-Gedrite Solvus. Am Mineral 56:1005–1041
- Rogowitz A, Huet B (2021) Evolution of fluid pathways during eclogitization and their impact on formation and deformation of eclogite: A microstructural and petrological investigation at the type locality (Koralpe, Eastern Alps, Austria). Tectonophysics 819:229079. https://doi.org/10.1016/j.tecto.2021.229079
- Rooney TP, Riecker RE, Gavasci AT (1975) Hornblende deformation features. Geology 3:364–366. https://doi.org/10.1130/0091-7613(1975)3%253C364:HDF%253E2.0.CO;2
- Rybacki E, Dresen G (2000) Dislocation and diffusion creep of synthetic anorthite aggregates. J Geophys Res Solid Earth 105:26017–26036. https://doi.org/10.1029/2000JB900223
- Rybacki E, Dresen G (2004) Deformation mechanism maps for feldspar rocks. Tectonophysics 382:173–187. https://doi.org/10.1016/j.tecto.2004.01.006
- Schmid SM, Casey M (1986) Complete fabric analysis of some commonly observed quartz c-axis patterns. Miner Rock Deform Lab Stud Geophys Monogr Ser 36:263–286. https://doi.org/10.1029/GM036p0263

- Scott JM, Konrad-Schmolke M, O'brien PJ, Günter C (2013) High-T, Low-P Formation of Rare Olivine-bearing Symplectites in Variscan Eclogite. J Petrol 54:1375–1398. https://doi.org/10.1093/petrology/egt015
- Shigematsu N, Tanaka H (2000) Dislocation creep of fine-grained recrystallized plagioclase under low-temperature conditions. J Struct Geol 22:65–79. https://doi.org/10.1016/S0191-8141(99)00132-7
- Sikdar A, Dutta D, Misra S (2023) Superplastic deformation inside the knife-sharp shear bands in mid-crustal granites. J Struct Geol 177:104980. https://doi.org/10.1016/j.jsg.2023.104980
- Skemer P, Katayama I, Jiang Z, Karato S (2005) The misorientation index: Development of a new method for calculating the strength of lattice-preferred orientation.

 Tectonophysics 411:157–167. https://doi.org/10.1016/j.tecto.2005.08.023
- Skrotzki W (1992) Defect structure and deformation mechanisms in naturally deformed hornblende. Phys Status Solidi A 131:605–624. https://doi.org/10.1002/pssa.2211310232
- Skrotzki W (1990) Microstructure in hornblende of a mylonitic amphibolite. In: Knipe RJ, Rutter EH (eds) Deformation Mechanisms, Rheology and Tectonics. Geological Society of London Special Publications. pp 321–325
- Soret M, Agard P, Ildefonse B, et al (2019) Deformation mechanisms in mafic amphibolites and granulites: record from the Semail metamorphic sole during subduction infancy. Solid Earth 10:1733–1755. https://doi.org/10.5194/se-10-1733-2019
- Spear FS (1981) An experimental study of hornblende stability and compositional variability in amphibolite. Am J Sci 281:697–734. https://doi.org/10.2475/ajs.281.6.697
- Spear FS (1993) Metamorphic phase equilibria and pressure-temperature-time paths. Mineral Soc Am Monogr 799:
- Spencer DA, Tonarini S, Pognante U (1995) Geochemical and Sr-Nd isotopic characterisation of Higher Himalayan eclogites (and associated metabasites). Eur J Mineral 89–102. https://doi.org/10.1127/ejm/7/1/0089
- Spruzeniece L, Piazolo S, Daczko NR, et al (2017) Symplectite formation in the presence of a reactive fluid: insights from hydrothermal experiments. J Metamorph Geol 35:281–299. https://doi.org/10.1111/jmg.12231
- Spry A (1969) Metamorphic Textures. Pergamon
- Stipp M, Stünitz H, Heilbronner R, Schmid SM (2002) The eastern Tonale fault zone: a 'natural laboratory' for crystal plastic deformation of quartz over a temperature range from 250 to 700°C. J Struct Geol 24:1861–1884. https://doi.org/10.1016/S0191-8141(02)00035-4
- Štípská P, Powell R (2005) Constraining the P–T path of a MORB-type eclogite using pseudosections, garnet zoning and garnet-clinopyroxene thermometry: an example from the Bohemian Massif. J Metamorph Geol 23:725–743. https://doi.org/10.1111/j.1525-1314.2005.00607.x

- Stöckhert B (2002) Stress and deformation in subduction zones: insight from the record of exhumed metamorphic rocks. In: De Meer S, Drury MR, de Bresser JHP, Pennock GM (eds) Deformation Mechanisms, Rheology and Tectonics: Current Status and Future Perspectives. Geological Society of London Special Publications. pp 255–274
- St-Onge MR, Rayner N, Palin RM, et al (2013) Integrated pressure-temperature-time constraints for the Tso Morari dome (Northwest India): implications for the burial and exhumation path of UHP units in the western Himalaya. J Metamorph Geol 31:469–504. https://doi.org/10.1111/jmg.12030
- Stout JH (1972) Phase Petrology and Mineral Chemistry of Coexisting Amphiboles from Telemark, Norway. J Petrol 13:99–145. https://doi.org/10.1093/petrology/13.1.99
- Straume, Austrheim (1999) Importance of fracturing during retro-metamorphism of eclogites. J Metamorph Geol 17:637–652. https://doi.org/10.1046/j.1525-1314.1999.00218.x
- Svahnberg H, Piazolo S (2010) The initiation of strain localisation in plagioclase-rich rocks: Insights from detailed microstructural analyses. J Struct Geol 32:1404–1416. https://doi.org/10.1016/j.jsg.2010.06.011
- Tatham DJ, Lloyd GE, Butler RWH, Casey M (2008) Amphibole and lower crustal seismic properties. Earth Planet Sci Lett 267:118–128. https://doi.org/10.1016/j.epsl.2007.11.042
- Tichomirowa M, Köhler R (2013) Discrimination of protolithic versus metamorphic zircon ages in eclogites: Constraints from the Erzgebirge metamorphic core complex (Germany). Lithos 177:436–450. https://doi.org/10.1016/j.lithos.2013.07.013
- Tokle L, Hirth G, Behr WM (2019) Flow laws and fabric transitions in wet quartzite. Earth Planet Sci Lett 505:152–161. https://doi.org/10.1016/j.epsl.2018.10.017
- Tullis J, Yund RA (1980) Hydrolytic weakening of experimentally deformed Westerly granite and Hale albite rock. J Struct Geol 2:439–451. https://doi.org/10.1016/0191-8141(80)90005-X
- Vernon RH (ed) (2018) Microstructures of Deformed Rocks. In: A Practical Guide to Rock Microstructure, 2nd edn. Cambridge University Press, Cambridge, pp 228–352
- Wang X, Zhang JF, Tommasi A, et al (2023) Experimental Evidence for a Weak Calcic-Amphibole-Rich Deep Crust in Orogens. Geophys Res Lett 50:e2022GL102320. https://doi.org/10.1029/2022GL102320
- Warren CJ (2013) Exhumation of (ultra-)high-pressure terranes: concepts and mechanisms. Solid Earth 4:75–92. https://doi.org/10.5194/se-4-75-2013
- Wawrzenitz N, Romer RL, Grasemann B, Morales LG (2019) Pre-UHP titanite archives proand retrograde episodes of fluid-marble-interaction (Dabie Shan UHP unit, China). Lithos 350–351:105232. https://doi.org/10.1016/j.lithos.2019.105232
- Wayte GJ, Worden RH, Rubie DC, Droop GTR (1989) A TEM study of disequilibrium plagioclase breakdown at high pressure: the role of infiltrating fluid. Contrib Mineral Petrol 101:426–437. https://doi.org/10.1007/BF00372216

- Wex S, Mancktelow NS, Hawemann F, et al (2018) Inverted distribution of ductile deformation in the relatively "dry" middle crust across the Woodroffe Thrust, central Australia. Solid Earth 9:859–878. https://doi.org/10.5194/se-9-859-2018
- White SH, Knipe RJ (1978) Transformation- and reaction-enhanced ductility in rocks. J Geol Soc 135:513–516. https://doi.org/10.1144/gsjgs.135.5.0513
- Whitney DL, Evans BW (2010) Abbreviations for names of rock-forming minerals. Am Mineral 95:185–187. https://doi.org/10.2138/am.2010.3371
- Wilke FDH, O'Brien PJ, Schmidt A, Ziemann MA (2015) Subduction, peak and multi-stage exhumation metamorphism: Traces from one coesite-bearing eclogite, Tso Morari, western Himalaya. Lithos 231:77–91. https://doi.org/10.1016/j.lithos.2015.06.007
- Will TM, Schmädicke E (2001) A first find of retrogressed eclogites in the Odenwald Crystalline Complex, Mid-German Crystalline Rise, Germany: evidence for a so far unrecognised high-pressure metamorphism in the Central Variscides. Lithos 59:109–125. https://doi.org/10.1016/S0024-4937(01)00059-7
- Wilson CJL (1975) Preferred Orientation in Quartz Ribbon Mylonites. GSA Bull 86:968–974. https://doi.org/10.1130/0016-7606(1975)86%253C968:POIQRM%253E2.0.CO;2
- Xia F, Brugger J, Ngothai Y, et al (2009) Three-Dimensional Ordered Arrays of Zeolite Nanocrystals with Uniform Size and Orientation by a Pseudomorphic Coupled Dissolution–Reprecipitation Replacement Route. Cryst Growth Des 9:4902–4906. https://doi.org/10.1021/cg900691a
- Zertani S, Morales LFG, Menegon L (2024) Omphacite breakdown: nucleation and deformation of clinopyroxene-plagioclase symplectites. Contrib Mineral Petrol 179:44. https://doi.org/10.1007/s00410-024-02125-0
- Zhang J, Green HW, Bozhilov KN (2006) Rheology of omphacite at high temperature and pressure and significance of its lattice preferred orientations. Earth Planet Sci Lett 246:432–443. https://doi.org/10.1016/j.epsl.2006.04.006
- Zhang Z-M, Shen K, Sun W-D, et al (2008) Fluids in deeply subducted continental crust: Petrology, mineral chemistry and fluid inclusion of UHP metamorphic veins from the Sulu orogen, eastern China. Geochim Cosmochim Acta 72:3200–3228. https://doi.org/10.1016/j.gca.2008.04.014
- Zhao S, Jin Z, Zhang J, et al (2012) Does subducting lithosphere weaken as it enters the lower mantle? Geophys Res Lett 39:. https://doi.org/10.1029/2012GL051666